Statement

The work contained in this thesis titled **'Study of Laser Induced Resonance and Coalescence using Non-Hermitian Quantum Mechanics'** has been carried out by me under the supervision of Dr. Ashish K. Gupta, Associate Professor, Department of Chemistry, Indian Institute of Technology Guwahati. This work has not been submitted elsewhere for the award of any degree.

Dhruba Jyoti Kalita

IIT Guwahati

October,2011

Certificate

It is certified that the work contained in the thesis entitled **'Study of Laser Induced Resonance and Coalescence using Non-Hermitian Quantum Mechanics'** by Dhrubam Jyoti Kalita, a student of Department of Chemistry, Indian Institute of Technology Guwahati, for the award of the degree of Doctor of Philosophy has been carried out under my supervision. This work has not been submitted elsewhere for any degree.

Ashish K. Gupta

Associate Professor,
Department of Chemistry
IIT Guwahati
Guwahati - 781039, India
October,2011

To
My parents.....

Acknowledgments

This thesis might not have seen through its completion unless I had the support and encouragement of numerous people around me. Today, when I bring it to an end, I would like to express few words of appreciation to the people who actually made this thesis a reality and an unforgettable experience for me. To begin with, I would like to thank my supervisor, Dr. Ashish Kumar Gupta not only for being so supportive, but also for providing me with the opportunity to travel and interact with people who inspired me to work even harder and pursue science more vigorously. Without him, and his ability to raise my spirits whenever I was the most discouraged, I could have never made it this far. Always allowing me to pursue my research the way I desired, he gave me the opportunity to learn from my mistakes being always there by me in all my troubles. In my countless discussion sessions with him which I am going to treasure forever, he not only showed how science and its challenges could be made interesting to ease out a solution, but also taught me the way this fun could be conveyed to the others.

I sincerely thank and appreciate the members of my doctoral committee, Prof. Jubaraj Bikash Baruah, Dr. Charudatt Y Kadolkar, Dr. Aditya N. Panda and Dr. Manabendra Sarma for periodically assessing my work and providing many detailed and crucial comments for its betterment.

I am going to cherish my time spent in IITG due to the many friends and groups - whom I consider a part of my life. Things around me wouldn't have been so beautiful if I wouldnt have met and shared my moments with Krishna da, Gunin da, Pras-

anta da, Ballav da, Sonit da, Prasenjit, Rupam, Bimlesh, Musawwer, Moushumi and Raihana. My time in IITG was enriched by my juniors Sayak, Dip, Bhaskar, Renjith, Paramartha, Jiban, Aswini, Apurba, Rahul, Subrata, Somnath, Anupal, Tridip, Abhijit, Arunangshu, Amey, Akshay and Ishir.

I am thankful to Prof. Lorenz S.Cederbaum of Heidelberg University, Germany for various constructive suggestions towards the improvement of my work. I consider myself lucky enough to be able to meet and interact with some of the finest interdisciplinary researchers during my PhD tenure when I participated in the Gordon Research Conference in USA.

I gratefully acknowledge the funding sources that made my PhD work possible. I was initially funded by Indian Institute of Technology Guwahati and latter received financial assistance from Council of Scientific and Industrial Research (CSIR), India. I gratefully acknowledge Department of Science and Technology, India for giving me opportunity to attend Gordon Research Conference. This thesis wouldn't have seen the light of this day without the care and encouragement of my teachers from B. Borooah College, Guwahati. I would like to thank Dr. Diganta Chowdhury, Dr. Dhrubajyoti Chowdhuri, and Mrs. Sutopa Raichaudhury for their teachings and constant motivation which made me reach this point. I take this opportunity to thank Prof. A. K. Mishra and Prof F. A. Ahmed of Department of Chemistry, Gauhati University for all their guidance during my Masters.

Finally, I would like to thank my family for their understanding, encouragement and patience in my every endeavor. My parents, my elder sister and brother have given me the strength towards this accomplishment throughout, as always, for which, I believe, mere expression of gratitude likewise doesnt suffice. I finally take the opportunity to remember my late beloved grandma for her blessings. A famous quote reads - "every journey begins with a single step" - and today, only because of my family, I move a step uphill towards my zenith.

Dhruba

Contents

List of Figures

List of Tables

Chapter 1

INTRODUCTION

High-intensity photoionization experiments on atoms and small molecules irradiated by intense laser light have received considerable interest. At intensities above ($\sim$) 10 TW/cm^2, atoms exhibit "above-threshold" ionization (ATI). ATI occurs when the atom absorbs more photons than necessary to dissociate the chemical bond [1, 29]. Molecules also exhibit ATI, but due to its additional degrees of freedom, other phenomena like multiphoton dissociation (MPD) and dissociative ionization takes place [35, 40, 53]. As the simplest molecule, the hydrogen molecular ion H_2^+ is of fundamental importance in molecular physics. The interaction of H_2^+ with intense ultrafast laser light pulses has revealed novel phenomena viz. bond softening and bond hardening in light induced molecular potentials [56]. The objective of my work is:

- To study the different resonance states of H_2^+ molecule by applying smooth exterior scaling (SES) method (**Chapter 2**).

- To perform better scaling, the existing SES method is modified. The different resonance states of H_2^+ molecule are studied with the help of this new method (**Chapter 3**).

- Parametric equations of motion (PEM) are implemented along with the SES

method to study the different resonance states of H_2^+ molecule (**Chapter 4**).

- To study the resonance coalescence in H_2^+ by applying PEM (**Chapter 5**).

1.1 What is a resonance state?

As mentioned by Taylor in his book on scattering theory [74] resonances are the most striking phenomenon in the whole range of the scattering experiment-perhaps one of the most striking events in nature. Resonances are associated with metastable states of a system which has sufficient energy to break up into two or more subsystems. Resonance positions and widths, E_r and Γ , respectively, are associated with the real and imaginary parts of the complex eigen values of the Schrödinger equation. Moiseyev, in his physics report [42] as well as in his book [44] has extensively discussed different kinds of resonances that occur in nature.

1.2 How do we get a resonance state?

To describe a quantum mechanical system the Hamiltonian acts as the central operator as it determines both the structural and the dynamical properties of the system. Usually the Hamiltonian is constructed as a Hermitian operator. Thus its eigenvalues are real. In most cases, the global dynamics is described by means of Hermitian Hamiltonian for the full system which considers explicitly all the particles, degrees of freedom and the complete space of states involved. But, for practical purposes, this exhaustive description may be impossible or in other words too detailed to carry out. This kind of difficulty may be overcome by taking a reduced description for the selected subspace and can be performed with effective Schrödinger equation. In this regime, the complementary subspace is taken into account by means of an effective interaction described by a non-Hermitian complex potential. According to the conventional (i.e., Hermitian) quantum mechanics a resonance state is associ-

ated with a wavepacket [44]. However, non-Hermitian quantum mechanics implies that each one of the resonance states is associated with a single square-integrable eigenstate of the complex-scaled Floquet operator [42, 57]. Owing to its asymptotic divergence behaviour, the resonance eigenfunctions don't belong to the Hermitian domain of the Hamiltonian. It was proved that by scaling the "reaction" coordinate (by carrying out a dilation transformation), the resonance wavefunction becomes square integrable [42]. This kind of scaling was done by applying complex coordinate method (CCM).

1.2.1 Complex coordinate (scaling) method (CCM or CSM)

Balslev et al. [2] and Simon [71] applied the CSM to study the molecular resonances within the framework of the Born-Oppenheimer approximation . The complex scaling method (CSM) is one of the useful methods for the determination of bound and unbound states. In CSM, internal coordinate r and wave number k are dilated by a complex factor as [41]

$$U(\theta) : r \to r\exp(i\theta), k \to k\exp(-i\theta).$$

Where $U(\theta)$ is a scaling operator and θ is a real number known as the scaling parameter. Under this transformation, the asymptotic divergent behavior $\exp(ik_r r)$ of a resonance state with a complex wave number $k_r = \kappa - i\gamma$ is changed into a damping form $\exp\left[i(\kappa - i\gamma)\right](r\cos\theta + ir\sin\theta) = exp\left[(\gamma\cos\theta - \kappa\sin\theta)r\right].\exp\left[i(\kappa\cos\theta + \gamma\sin\theta)r\right]$ for $\theta > \tan^{-}1\left(\frac{\gamma}{\kappa}\right)$. Therefore resonance states and bound states are obtained as discrete solutions of the following complex scaled Schrödinger equation:

$$H(\theta)\phi^{\theta} = E\phi^{\theta}$$

where $H(\theta) = U(\theta)HU^{-1}(\theta)$. Thus, taking the appropriate scaling parameter θ (in addition to bound states), we can solve resonance states by using squared-integrable basis functions ϕ_n;

$$\phi^{\theta} = \sum_{n=1}^{N} c_n \phi_n.$$

CCM causes no unphysical perturbation. However, it requires the analytical continuation of the scattering potential. As a result technical difficulties will often arise.

1.2.2 Complex absorbing potential (CAP)

Artificial reflections resulting from the use of the finite basis (grid) approximation are a major problem encountered in molecular physics. These reflections deteriorate the quality of the computational results. To remove such kind of reflections during simulation, it is necessary to impose some sort of absorbing-boundary conditions which provide outgoing waves in the asymptotic limit. This absorbing-boundary condition arises due to the addition of some kind of potential term to the Hamiltonian. In the literature these kind of potentials are called optical potentials [20,21,49,50,55]. Optical potentials have been used for a long time in nuclear physics. Later on, Riss and Meyer replaced the term optical potential by complex absorbing potential (CAP) [59]. CAP is located in the asymptotic region where the motion becomes free and generates an absorbing region that annihilates outgoing wavepackets and as a result prevents undesired reflections. CAP avoids artificial reflections occuring at the grid boundary and allows simulations of large-scale strongly coupled scattering problems which involve millions of basis functions [36,48,79]. However, CAP leads to the artificial perturbations of the system due to its non-physical nature.They not only absorb the wavepacket, but also produce reflections themselves. Hence it is essential to minimize these reflections which is troublesome [28,49,50]. But besides this difficulty, the CAP method stands out due to its straightforward and simple applicability. CAP makes resonance wavefunctions square integrable like the CCM. But CAP doesn't

require the analytical continuity of the scattering potential. Moreover, it was observed that by incorporating the CAP, the absorption of the flux can be increased [11]. This fact was later supported by the series of papers, where different improvements of CAPs were studied [60–62]. The CAP is zero in the interaction region and "turns on" in the region where there is no interaction. Recently CAP has been successfully and efficiently used for the calculation of electronic resonances in atomic and molecular systems [10,47,65,68] and for wavepacket propagation [10,47,65]. This method is also used in the time dependent treatment of reactive scattering to calculate the reaction probabilities [49, 50, 69]. However, CAPs can not give convergent results in case of multichannel decay [43].

It is also possible to generate the absorbing areas by other techniques (besides CAP) such as those based on CCM or CSM (mentioned in **1.2.1**). The CSM is transformative. It consists of an unbounded similarity transformation of the Hamilton operator [34]. But CSM requires analytical continuation of the scattering potential, thus giving rise to some technical difficulties. To remove these problems, a large number of methods have been proposed by various researchers so far [18, 33, 39, 72]. These methods include exterior complex scaling method (ECS) and smooth exterior scaling method (SES).

1.2.3 Exterior complex scaling (ECS)

The CSM method can not be applied where the potential of the system is not dilation analytic (i.e., can not be expanded in the Taylor series expansion). The resonances of nondilation analytic potentials can be obtained numerically by using exterior complex scaling (ECS) procedure proposed by Nicolaides [51] and Simon [72]. According to them the coordinates are kept unscaled in the region where the potential is not dilation analytic and scaling is done in the external region where the potential is dilation

analytic. The scaled Hamiltonian has the following form:

$$\hat{H}_\theta = \begin{cases} \hat{H}(x) & if \quad x < x_0 \\ \hat{H}\left((x - x_0)\, e^{i\theta}\right) & if \quad x > x_0 \end{cases} \tag{1.1}$$

Here x_0 is the point where complex scaling is introduced. Resonances are obtained as the eigen functions of $\hat{H}_\theta$

$$\hat{H}_\theta \Psi_{res} = (E_r - \frac{i}{2}\Gamma)\Psi_{res}.$$

1.2.4 Smooth exterior scaling (SES)

Smooth exterior scaling (SES) method is a variant of CSM. Here, the complex path is chosen in such a way that the complex scaling path is followed within the asymptotic limit. SES does not touch the interaction region and its effect "turns-on" only close to the end of the grid. In CSM, the molecular potential energy surface (PES) must be complex scaled in the interaction region. On the other hand, the potential need not be scaled in the region where there is no interaction. But in SES, the scaling is done in the non-interaction region and hence, no scaling is required for the potential. Out of all these scaling methods mentioned, SES is the most flexible one [9, 25, 26, 43, 63, 75]. By applying SES similarity transformations to the Hamiltonian, it is possible to generate reflection free complex absorbing potentials (RF CAPS) [70]. SES also shares the property of the CAP (i.e., it leaves the interaction region unaffected and only "turns-on" close to the end of the grid). It also shares the rigorous mathematical foundation of CSM. In the SES method, the wavepacket is allowed to propagate along an arbitrary (smooth) path in the complex coordinate plane and gets absorbed when the path leaves the real axis. It is the most efficient method for the production of RF CAPs. It is simple to implement and avoids most of the perturbation of the physical system.

The Moiseyev-Hirschfelder generalization [46] of the complex coordinate method

associated the resonance poles of the S-matrix, $E = E_r - iE_i$, with the θ independent complex eigenvalues of $\hat{H}$:

$$\hat{H}\Psi = E\Psi, \tag{1.2}$$

where

$$\hat{H} = \frac{-\hbar^2}{2M}\frac{\partial^2}{\partial z^2} + V(z). \tag{1.3}$$

Here $z = F(x)$ is a path in the complex coordinate plane and is given by

$$z = F(x) \longrightarrow x\exp(i\theta) \quad \text{as} \quad x \longrightarrow \infty \tag{1.4}$$

The smooth-exterior-scaling path is defined as [63]

$$f(x) = \frac{\partial F}{\partial x} = 1 + [\exp(i\theta) - 1]g(x), \tag{1.5}$$

where $g(x)$ is varied from 0 to 1 around the point x=x_0. When $V(x \geq x_0)$=0 , unscaled potential $V(x)$ can be used instead of complex potential $V(z)$. The smooth-exterior-scaled Hamiltonian is given as follows [25, 43, 58] :

$$\hat{H} = \frac{-\hbar^2}{2M}\frac{\partial^2}{\partial x^2} + V[F(x)] + \hat{V}_{CAP}. \tag{1.6}$$

where,

$$\hat{V}_{CAP} = \frac{1}{2}V_1(x)\frac{\partial}{\partial x} + V_2(x)\frac{\partial^2}{\partial x^2}, \tag{1.7}$$

and,

$$V_1(x) = \frac{\hbar^2}{Mf^3(x)}\frac{\partial f(x)}{\partial x}, \tag{1.8}$$

$$V_2(x) = \frac{\hbar^2}{2M}(1 - f^{-2}(x)). \tag{1.9}$$

The volume element is given by

$$dz = f(x)dx \tag{1.10}$$

To simplify the expression of the volume element (i.e. to make $dz = dx$) one can transform the Hamiltonian by defining a function Φ,

$$\Psi(x) = f^{-1/2}\Phi(x), \tag{1.11}$$

such that

$$\hat{H}_f = \frac{-\hbar^2}{2M}\nabla_f^2 + V[F(x)], \tag{1.12}$$

where,

$$\nabla_f^2 = f^{1/2}(x)\frac{\partial^2}{\partial z^2}f^{-1/2}(x). \tag{1.13}$$

Here, $\Phi(x)$ is an eigenfunction of $\hat{H}_f$. Now $\hat{H}_f$ can be redefined as,

$$\hat{H}_f = \frac{-\hbar^2}{2M}\frac{\partial^2}{\partial x^2} + V[F(x)] + \hat{V}_{CAP}^f, \tag{1.14}$$

where,

$$\hat{V}_{CAP}^f = V_0(x) + V_1(x)\frac{\partial}{\partial x} + V_2(x)\frac{\partial^2}{\partial x^2}, \tag{1.15}$$

and,

$$V_0(x) = \frac{\hbar^2}{4M}f^{-3}(x)\frac{\partial^2 f}{\partial x^2} - \frac{5\hbar^2}{8M}f^{-4}(x)\left(\frac{\partial f}{\partial x}\right)^2. \tag{1.16}$$

Now $g(x)$ (in equation 1.5) can be defined with the help of a specific family of integration paths in the complex coordinate plane as follows:

$$g(x) = 1 + 0.5\left[\tanh(\lambda(x - x_0)) - \tanh(\lambda(x + x_0))\right]. \tag{1.17}$$

The path derived from $g(x)$ (given in equation 1.17) will be referred as Moiseyev path. By carrying out integration over $g(x)$, the complex path (i.e. Moiseyev path) $F(x)$ is obtained. $F(x)$ has the following form:

$$F(x) = x + (e^{i\theta} - 1)\left[x + \frac{1}{2\lambda}\ln\frac{\cosh[\lambda(x - x_0)]}{\cosh[\lambda(x + x_0)]}\right]. \tag{1.18}$$

The CAP terms are calculated by using the expression for $g(x)$ given in equation 1.17 and incorporating the following analytical expressions for the first and second derivatives of $f(x)$:

$$\frac{\partial f}{\partial x} = 0.5\lambda(e^{i\theta} - 1)\left[\frac{1}{\cosh^2(\lambda(x - x_0))} - \frac{1}{\cosh^2(\lambda(x + x_0))}\right] \tag{1.19}$$

$$\begin{aligned}\frac{\partial^2 f}{\partial x^2} = \lambda^2(e^{i\theta} - 1)\Bigg[&\frac{1}{\cosh^2(\lambda(x + x_0))}\tanh(\lambda(x + x_0)) \\ &- \frac{1}{\cosh^2(\lambda(x - x_0))}\tanh(\lambda(x - x_0))\Bigg].\end{aligned} \tag{1.20}$$

There are other complex paths that can also be used in the calculation and these are given below:

Wood-Saxon path [25]:

$$g(x) = (1 + e^{(x_0 - x)\lambda})^{-1} + (1 + e^{(x_0 + x)\lambda})^{-1} \tag{1.21}$$

$$F(x) = x + (e^{i\theta} - 1)\left[2x - \frac{1}{\lambda}\ln(1 + e^{(x_0 + x)\lambda}) + \frac{1}{\lambda}\ln(1 + e^{(x_0 - x)\lambda})\right] \tag{1.22}$$

Taylor path [25]:

$$\begin{aligned}g(x) =&(1 + e^{(x_0 - x)\lambda})^{-1} + (1 + e^{(x_0 + x)\lambda})^{-1} \\ &+x\lambda\left[e^{(x_0 - x)\lambda}(1 + e^{(x_0 - x)\lambda})^{-2} - e^{(x_0 + x)\lambda}(1 + e^{(x_0 + x)\lambda})^{-2})\right]\end{aligned} \tag{1.23}$$

$$F(x) = x + (e^{i\theta} - 1)x\left[(1 + e^{\lambda(x_0 - x)})^{-1} + (1 + e^{\lambda(x_0 + x)})^{-1}\right] \tag{1.24}$$

and

Elander-Yarevsky path [9]:

$$g(x) = \begin{cases} 0 & x \leq x_0 \\ 1 - e^{-\lambda(x - x_0)^2} + 2\lambda(x - x_0)^2 e^{-\lambda(x - x_0)^2} & x > x_0 \end{cases} \tag{1.25}$$

$$F(x) = \begin{cases} x & x \leq x_0 \\ x + (e^{i\theta} - 1)(x - x_0)(1 - e^{-\lambda(x-x_0)^2}) & x > x_0 \end{cases} \tag{1.26}$$

1.3 Floquet Theory

Periodicity of Hamiltonian is a special case of time-dependent Hamiltonian. For such case it is also possible to make certain general statements about the solution of the time-dependent Schrödinger equation. The theory of these systems is known as Floquet theory and its application to quantum mechanical systems was first introduced by Shirley in 1965.

Floquet theory provides a unique functional form for a Floquet propagator. It permits exact or approximate solutions for the semi-classical equations of motion without resorting to perturbation theory, the rotating wave approximation [17, 19], or to a brute force integration for times greater than one oscillation of the field. The periodic form of the Floquet propagator helps the reformulation of the problem with solutions and eigenvalues which characterize and determine the dynamics of the system. The eigenfunctions and the eigenvalues are in the form of Floquet exponents. The usefulness of the theory is evident by the diversity of its applications. Floquet theory had been applied to hydrogen atom multiphoton ionization by Salzman [66], Chu and Reinhardt [5, 6]. On the other hand, Floquet theory had been used to a "larger" system, the rotating diatomic by Leasure , Wyatt and Milfeld [30, 31].

1.3.1 Time-Dependent Floquet Theory

The usual Time-dependent Schrödinger equation (TDSE) has the following form:

$$i\hbar \frac{\partial \psi(t)}{\partial t} = \hat{H}(t)\psi(t), \tag{1.27}$$

where the Hamiltonian is periodic in time with period τ, that is,

$$\hat{H}(t) = \hat{H}(t+\tau).$$

Solution of the TDSE can be written as

$$\psi(t) = Te^{-i\hat{H}t}\psi_0,$$

where T is time ordering operator and ψ_0 is the initial wave function. Now we can define $\psi(\tau)$ as:

$$\psi(\tau) = U(0 \to \tau)\psi_0 = U_0\psi_0, \tag{1.28}$$

where $U(0 \to \tau)$ is time propagator for the time 0 to τ. We can also define

$$\psi(m\tau) = U\left[(m-1)\tau \to m\tau\right] U\left[(m-2)\tau \to (m-1)\tau\right] .....U(\tau \to 2\tau)U(\tau \to 0)\psi_0. \tag{1.29}$$

But H(t) is periodic in time and as a result

$$U(0,\tau) = U(\tau, 2\tau) = U\left[(m-1)\tau, m\tau\right].$$

Then equation 1.29 gives

$$\psi(m\tau) = U^m(0 \to \tau)\psi_0 = U_0^m\psi_0. \tag{1.30}$$

$\psi(t)$ in Floquet ansatz can be written as

$$\psi(t) = e^{\frac{-i\epsilon t}{\hbar}}\phi(t), \tag{1.31}$$

where, ϕ and ϵ are the Floquet vector and Floquet exponent respectively. ϕ is also periodic in time

$$\phi(t) = \phi(t + \tau).$$

By comparing equations 1.28, 1.30 and 1.31, we have,

$$e^{\frac{-i\epsilon\tau}{\hbar}}\phi(\tau) = U_0\psi_0. \tag{1.32}$$

But at initial time (t=0), equation 1.31 gives

$$\Psi_0 = \phi_0. \tag{1.33}$$

Therefore, equation 1.32 becomes

$$U_0\phi_0 = e^{\frac{-i\epsilon t}{\hbar}}\phi_0. \tag{1.34}$$

Equation 1.34 is the eigen value equation. Thus the Floquet vector and the exponent can be calculated by diagonalizing the one optical cycle propagator (in equation 1.34). Then by using equation 1.29, one can get the dynamics after any optical cycle later.

1.3.2 Time-Independent Floquet Theory [73]

The usual Time-dependent Schrödinger equation (TDSE) has the following form:

$$i\hbar\frac{\partial\Psi(x,t)}{\partial t} = \hat{H}(x,t)\Psi(x,t), \tag{1.35}$$

where the Hamiltonian is periodic in time with period T, that is,

$$\hat{H}(x, t + T) = \hat{H}(x, t).$$

In Floquet ansatz,

$$\Psi(x,t) = e^{-\frac{i\epsilon_\lambda t}{\hbar}}\phi_\lambda(x,t). \tag{1.36}$$

Substituting equation 1.36 into equation 1.35 and rearranging terms we get

$$\hat{H}_F(x,t)\phi_\lambda(x,t) = \epsilon_\lambda\phi_\lambda(x,t), \tag{1.37}$$

where $\hat{H}_F$ is called the Floquet Hamiltonian and has the following form:

$$\hat{H}_F(x,t) = \left[\hat{H}(x,t) - i\hbar\frac{\partial}{\partial t}\right]. \tag{1.38}$$

Here $\phi(x,t)$ and ϵ are called Floquet eigenstate and Floquet eigenvalue respectively. Equation 1.37 is an eigenvalue equation in two variables i.e., x and t. Here Floquet eigenstates, $\phi(x,t)$ are also time periodic with the same period T as the Hamiltonian. Equation 1.36 is a particular solution of the TDSE and its general solution is given as

$$\Psi(x,t) = \sum_\lambda a_\lambda e^{-\frac{i\epsilon_\lambda t}{\hbar}}\phi_\lambda(x,t). \tag{1.39}$$

Now we can always rearrange equation 1.36 as follows:

$$\begin{aligned}\Psi(x,t) &= e^{-\frac{i\epsilon_\lambda t}{\hbar}}\phi_\lambda(x,t),\\ &= e^{\frac{-i(\epsilon_\lambda + n\hbar\omega)t}{\hbar}}e^{in\omega t}\phi_\lambda(x,t).\end{aligned} \tag{1.40}$$

This rearrangement leads to a series of new Floquet eigenvalues , $\epsilon_\lambda + n\hbar\omega$ with corresponding eigenfunctions, $\phi_{\lambda n}(x,t) \equiv e^{in\omega t}\phi_\lambda(x,t)$. For integer value of n, $\phi_{\lambda n}(x,t)$ will also be time periodic so long as $\phi_\lambda(x,t)$ is.

1.3.3 Representation of the Floquet Hamiltonian

It will be possible to get a representation for the Floquet Hamiltonian using a complete basis in both position and time. Now as both $\phi_\lambda(x,t)$ and $\hat{H}(x,t)$ are periodic in time, they may be expanded in a Fourier series as follows:

$$\phi_\lambda(x,t) = \sum_{\beta m} \phi^m_{\beta\lambda} e^{im\omega t}|\beta\rangle, \tag{1.41}$$

$$\langle\alpha|\hat{H}|\beta\rangle = \sum_n \hat{H}^n_{\alpha\beta} e^{in\omega t}. \tag{1.42}$$

Now, substitution of equations 1.41 and 1.42 into the Schrödinger equation, one obtains an infinite set of relations for $\phi^{(n)}_{\alpha\lambda}$:

$$\sum_{\beta m} \langle\langle \alpha n|\hat{H}_F|\beta m\rangle\rangle \phi^{(m)}_{\beta\lambda} = \epsilon_\lambda \phi^{(n)}_{\alpha\lambda}, \tag{1.43}$$

where $\hat{H}_F$ is the time-independent Floquet Hamiltonian with matrix elements:

$$\langle\langle \alpha n|\hat{H}_F|\beta m\rangle\rangle = \langle\langle \alpha n|\hat{H}|\beta m\rangle\rangle + \langle\langle \alpha n| - i\hbar\frac{\partial}{\partial t}|\beta m\rangle\rangle, \tag{1.44}$$

$$= H^{(n-m)}_{\alpha\beta} + \delta_{\alpha\beta}\langle n| - i\hbar\frac{\partial}{\partial t}|m\rangle, \tag{1.45}$$

$$= H^{(n-m)}_{\alpha\beta} + n\hbar\omega\delta_{\alpha\beta}\delta_{nm}. \tag{1.46}$$

If form of H is

$$H = H_0 + V_0 \cos\omega t,$$

then structure of the Floquet Hamiltonian matrix given by equation 1.46 is shown below:

$[H_F]$=

A+2 ωI	$B^\dagger$	0	0	0
B	A+ωI	$B^\dagger$	0	0
0	B	A	$B^\dagger$	0
0	0	B	A-ωI	$B^\dagger$
0	0	0	B	A-2ωI

The matrix A on the diagonal consists of matrix elements of the time averaged Hamiltonian and is given by

$$A_{\alpha\beta} = \langle\langle \alpha 0|H(x,t)|\beta 0\rangle\rangle = \frac{1}{T}\int_0^T \langle\alpha|H(x,t)|\beta\rangle dt = \langle\alpha|\bar{H}(x)|\beta\rangle = \langle\alpha|H_0|\beta\rangle, \quad (1.47)$$

where $\bar{H}(x)$ signifies the time average of $H(x,t)$ and the basis functions α, β may be chosen to be eigenstates of $\bar{H}(x)$, in which case A is diagonal. In each diagonal block, the matrix A is repeated with a shift of $n\hbar\omega I$. The eigenstates of $\bar{H}(x)$ are also shifted by multiples of $\hbar\omega$ and are called "field-dressed states". The matrix B contains the Fourier component at frequency ω of the coupling between the basis functions which is induced by the periodic Hamiltonian. The matrix B is given by

$$B_{\alpha\beta} = \langle\langle \alpha 0|H(x,t)|\beta 1\rangle\rangle = \frac{1}{T}\int_0^T \langle\alpha|H(x,t)|\beta\rangle e^{i\omega t} dt = \frac{1}{T}\int_0^T \langle\alpha|V_0\cos\omega t|\beta\rangle e^{i\omega t}. \quad (1.48)$$

1.4 Parametric equations of motion (PEM)

In parametric equations of motion [54], the Schrödinger equation is explicitly solved only once and then the solutions at other parameter values are obtained by propagating a set of ordinary differential equations through the parameter space of the Hamiltonian. Hence, it is possible to predict the wavefunction dynamics for an arbitrary range of field amplitudes and wavelengths. Initially, these kind of equations had been applied in the field of quantum chaos [54,76,77]. Rabitz and co-workers [38]

applied PEM to several simple, illustrative examples.

1.4.1 Derivation of Parametric equations of motion

Let us Consider an eigen value problem

$$\bar{\bar{H}}\bar{C_i}^R = \bar{C_i}^R E_i, \tag{1.49}$$

$$(\bar{C_i^L})^T \bar{\bar{H}} = E_i(\bar{C_i}^L)^T, \tag{1.50}$$

where $\bar{\bar{H}}$ depends linearly on parameter λ as

$$\bar{\bar{H}} = \bar{\bar{H}}_0 + \lambda\bar{\bar{V}},$$

where $\bar{\bar{H}}_0$ and $\bar{\bar{V}}$ are λ independent matrices and $\bar{C_i^R}$, $\bar{C_i^L}$ are the respective right and left eigen vectors of the complex general matrix $\bar{\bar{H}}$ having complex eigen values E_i. Superscript T stands for transpose. $\bar{C_i^R}$ and $\bar{C_i^L}$ follows the relationship

$$(\bar{C_i^L})^T \bar{C_i^R} = 1. \tag{1.51}$$

Equation 1.49 can be rewritten as

$$(\bar{\bar{H}}_0 + \lambda\bar{\bar{V}})\bar{C_n}^R = E_n\bar{C_n}^R. \tag{1.52}$$

Differentiating equation 1.52 with respect to λ and rearranging the terms, we have

$$\left[(\bar{\bar{H}}_0 + \lambda\bar{\bar{V}}) - E_n\right]\frac{\partial\bar{C_n^R}}{\partial\lambda} = \left[\frac{\partial E_n}{\partial\lambda} - \bar{\bar{V}}\right]\bar{C_n^R}. \tag{1.53}$$

Multiplying equation 1.53 by $(\bar{C_n^L})^T$ from both sides we get

$$(\bar{C_n^L})^T\left[(\bar{\bar{H}}_0 + \lambda\bar{\bar{V}}) - E_n\right]\frac{\partial\bar{C_n^R}}{\partial\lambda} = (\bar{C_n^L})^T\left[\frac{\partial E_n}{\partial\lambda} - \bar{\bar{V}}\right]\bar{C_n^R}. \tag{1.54}$$

Now rearranging the terms in equation 1.54 and using equation 1.52 and 1.51 we get

$$\frac{\partial E_n}{\partial \lambda} = V_{nn}, \tag{1.55}$$

where $(\bar{C}_n^L)^T \bar{\bar{V}} \bar{C}_n^R = V_{nn}$.

Multiplying equation 1.53 by $(\bar{C}_m^L)^T$ and using equation 1.51, we get

$$(\bar{C}_m^L)^T \left[E_m - E_n\right] \frac{\partial \bar{C}_n^R}{\partial \lambda} = \frac{\partial E_n}{\partial \lambda} \left[(\bar{C}_m^L)^T \bar{C}_n^R\right] - (\bar{C}_m^L)^T \bar{\bar{V}} \bar{C}_n^R. \tag{1.56}$$

After applying orthogonality condition (1.51), equation 1.56 can be rewritten as

$$(\bar{C}_m^L)^T \frac{\partial \bar{C}_n^R}{\partial \lambda} = -\frac{V_{mn}}{E_m - E_n}. \tag{1.57}$$

Multiplying equation 1.57 by $\bar{C}_m^R$ from both sides and summing over all m we get

$$\sum_{m \neq n} \bar{C}_m^R (\bar{C}_m^L)^T \left[\frac{\partial \bar{C}_n^R}{\partial \lambda}\right] = \sum_{m \neq n} -\frac{V_{mn} \bar{C}_m^R}{E_m - E_n}. \tag{1.58}$$

Using completeness of the basis, equation 1.58 can be rewritten as

$$\frac{\partial \bar{C}_n^R}{\partial \lambda} = \sum_{m \neq n} -\frac{V_{mn} \bar{C}_m^R}{E_m - E_n}, \tag{1.59}$$

Similarly,

$$\frac{\partial (\bar{C}_n^L)^T}{\partial \lambda} = \sum_{m \neq n} -\frac{V_{mn} \bar{C}_m^L}{E_m - E_n}, \tag{1.60}$$

where,

$$V_{mn} = (\bar{C}_m^L)^T \bar{\bar{V}} \bar{C}_n^R. \tag{1.61}$$

$\bar{\bar{V}}$ is not λ dependent whereas $\bar{\bar{V}}_{mn}$ depends linearly on λ. Differentiating equation

1.61 w.r.t λ we get

$$\frac{\partial V_{mn}}{\partial \lambda} = \frac{\partial (\bar{C}_m^L)^T}{\partial \lambda} \bar{\bar{V}} \bar{C}_n^R + (\bar{C}_m^L)^T \bar{\bar{V}} \frac{\partial \bar{C}_n^R}{\partial \lambda}. \tag{1.62}$$

Substituting $\frac{\partial \bar{C}_n^R}{\partial \lambda}$ and $\frac{\partial (\bar{C}_m^L)^T}{\partial \lambda}$ from equations 1.59 and 1.60 we get

$$\frac{\partial V_{mn}}{\partial \lambda} = \sum_{l \neq m} \frac{V_{lm} (\bar{C}_l^L)^T}{E_m - E_l} \bar{\bar{V}} \bar{C}_n^R + (\bar{C}_m^L)^T \bar{\bar{V}} \sum_{l \neq n} \frac{V_{ln} \bar{C}_l^R}{E_n - E_l}. \tag{1.63}$$

From the definition of V_{mn} we can write

$$\frac{\partial V_{mn}}{\partial \lambda} = \sum_{l \neq m} \frac{V_{ml} V_{ln}}{E_m - E_l} + \sum_{l \neq n} \frac{V_{ml} V_{ln}}{E_n - E_l}. \tag{1.64}$$

If we replace m by n in equation 1.64, we will get

$$\frac{\partial V_{nn}}{\partial \lambda} = \sum_{l \neq n} \frac{V_{nl} V_{ln}}{E_n - E_l} + \sum_{l \neq n} \frac{V_{nl} V_{ln}}{E_n - E_l}. \tag{1.65}$$

$$= 2 \sum_{l \neq n} \frac{V_{nl} V_{ln}}{E_n - E_l}, \tag{1.66}$$

$$= 2 \sum_{l \neq n} \frac{|V_{nl}|^2}{E_n - E_l}. \tag{1.67}$$

Collectively equations 1.55, 1.59, 1.60, 1.67 are called parametric equations of motion (PEM).

1.5 Thesis synopsis

To extensively investigate the different photodissociation mechanism of H_2^+ it is necessary to gather accurate information about the system which are coded into the wavefunctions. This accurate calculation of the states of the system necessitates the further development of the scaling techniques. We use the SES method and PEM through out the entire thesis to accurately study the resonance wavefunctions of H_2^+.

The main research results are detailed in four Chapters of this thesis, the contents of which can be outlined below-

Chapter 2 discusses the application of smooth exterior scaling method (SES) to study the time dependent dynamics of H_2^+ in intense laser field. In this method, the complex path is chosen in such a way that the complex scaling path is followed within the asymptotic limit. Here radial coordinate is scaled as

$$x \longrightarrow x\exp(i\theta) \quad \text{as} \quad x \longrightarrow \infty,$$

where θ is a real number known as the scaling parameter. We have constructed the SES Hamiltonian having form

$$\hat{H} = \frac{-\hbar^2}{2M}\frac{\partial^2}{\partial x^2} + V[F(x)] + \hat{V}_{CAP}.$$

All the terms appear in the Hamiltonian are discussed in **Chapter 1**. The resonance wavefunctions are calculated by diagonalizing this Hamiltonian. The wavefunctions calculated as a result provide indisputable proof in support of mechanisms for different phenomena happening during photodissociation. We report that one-photon dissociation takes place from ground vibrational state of H_2^+ at the intensity range of 10^{10} to 10^{14} W/cm^2. The multiphoton dissociation is dominant route for dissociation even at lower intensities. We have identified the bond-hardening states also.

In **Chapter 3**, we have developed a new variant of SES method to attain better absorption of the reflected wavepacket at the grid boundary. We name this new SES method as modified smooth exterior scaling method (MSES). In the proposed MSES method, scaling function, $\theta(x)$, is chosen as a real function rather than complex (as used in a conventional SES (CSES) method) and has spatial dependence. The usual implementation of SES begins by choosing a derivative of scaling path [F(x)], which is given by

$$f(x) = \frac{\partial F}{\partial x} = 1 + [exp(i\theta_0) - 1]g(x),$$

where θ_0 is the scaling parameter and g(x) goes smoothly from 0 to 1, resulting in f(x) going smoothly from 1 to $\exp(i\theta_0)$. Instead, we define the scaling path [F(x)] as

$$F(x) = xe^{i\theta(x)} = xe^{i\theta_0 g(x)},$$

where $\theta(x)$ goes smoothly from 0 to θ_0. This new method is then applied to study the time dependent dynamics of H_2^+ in intense laser field. We found that MSES is more computationally efficient compared to the CSES method.

Chapter 4 involves application of the parametric equations of motion (PEM) to study photodissociation dynamics of H_2^+. In the parametric equations of motion regime, the Schrödinger equation is explicitly solved only once and then the solutions at other parameter values are obtained by propagating a set of ordinary differential equations through the parameter space of the Hamiltonian. In this Chapter, we have treated amplitude and wavelength as parameters. Initial conditions to carry out the integration in the PEM regime, is given by SES method. Here we have studied how the different resonance states behave with respect to the change in field amplitude. The advantage of this method is that one can easily trace the different states that are changing as the field parameter changes. In this Chapter, we have shown that some higher lying vibrational states become bound states in continuum at higher field amplitudes.

In **Chapter 5**, we discuss the coalescence (exceptional point) phenomenon occuring between different field free vibronic resonance states of H_2^+ and continuum by applying PEM. At the coalescing point the two states become self-orthogonal. Hence spectrum of the system is incomplete which renders impossible to implement diagonalization method. Previously it was reported that coalescence occurs between field free vibronic states. In this Chapter, we have extensively studied this non-Hermitian quantum mechanical aspect and found that coalescence occurs between field free vibronic states as well as between vibronic states and continuum states.

Chapter 6 consists of conclusions of the thesis. We have so far discussed application of non-Hermitian quantum mechanics to study the different resonance states of H_2^+ molecular ion. Through out the thesis, we have performed radial scaling technique (SES) to the H_2^+ molecular ion. This scaling of the coordinate transforms the Hamiltonian from Hermitian to non-Hermitian. Moreover, SES generates reflection free complex absorbing potentials (RFCAP) which acts as an absorber of the artificial reflections occuring at the grid boundary. It has been shown that by modification of the SES method, absorbing quality of the complex absorbing potentials increases. Implementation of PEM in functional space helps to trace different eigen states as a function of field amplitude and wavelength. This Chapter concludes the thesis with the mention of our main research results.

Chapter 2

APPLICATION OF SMOOTH EXTERIOR SCALING METHOD TO STUDY THE TIME DEPENDENT DYNAMICS OF H_2^+ IN INTENSE LASER FIELD.

Intense ultrashot laser pulses are used to initiate and control molecular dynamics and have many applications in molecular science. It has been reported earlier that the H_2 and H_2^+ are the ideal systems for a detailed understanding of the ionization and dissociation dynamics of small molecules. Multiphoton dissociation (MPD) of H_2^+ have been studied extensively [3, 7, 12, 13, 67]. Many interesting phenomena viz. "bond-hardening" and "bond-softening" have been put forward. All these phenomena have been explained using one-photon dressed potential picture.

Smooth exterior scaling (SES) method is one of the best method to generate the wavefunctions without any artificial reflections occurring at the grid [9, 25, 26, 43, 63, 75]. Furthermore it doesn't disturb the interaction region. In this method, one can

keep as large a grid as desired, undisturbed by complex scaling. The wavefunctions calculated with this method can provide indisputable proof for different mechanisms. The dissociating channels can be recognized directly from the resonance wavefunctions. A resonance state is a long lived state that has sufficient energy to break-up into two or more subsystems. Continuum tails are part of the wavefunctions at large distances but still in the undisturbed region (due to the scaling).

In this Chapter, SES method is applied to the time-dependent dynamics problem [52, 70, 78]. We have calculated resonance energies and width of H_2^+ in intense laser field undergoing multiphoton dissociation (MPD). Chu et al. [7] have studied the same system using complex scaling method. The advantage of this method is that we can get undistorted resonance wavefunctions. We have discussed both complex scaling method (CSM) and SES method in **Chapter 1**.

2.1 Floquet formalism for model H_2^+ multiphoton dissociation (MPD)

We have applied the SES method on study of complex quasi vibrational energies (Resonance energies) of H_2^+, undergoing MPD in intense laser fields. The time dependent Schrödinger equation (TDSE) has the following form:

$$i\hbar\frac{\partial\psi(t)}{\partial t} = \hat{H}(t)\psi(t). \tag{2.1}$$

where,

$$\hat{H}(t) = \hat{H}_0 + \mu \cdot \epsilon_0 \cos\omega t,$$

Here, H_0 and μ are field free Hamiltonian and dipole operator respectively and ϵ_0 and ω are amplitude and frequency of the laser respectively.

We have applied Floquet ansatz (discussed in **Chapter 1**). Different Floquet channels can be interpreted as number of photons absorbed or required for stimulated

emission. We have used the "particle in a box basis functions". Box ends at 20 a.u. and the exterior scaling function [g(x)] is centered at 12 a.u. The solution of the time dependent Schrödinger equation can be written as- $\psi(t) = \exp\left(-i\epsilon^{QE}t\right)\phi(t)$, where $\phi(t)$ is a time periodic function. ϵ^{QE} and ϕ are the corresponding eigenvalue (quasi-energy) and eigenfunction (Floquet state) of the Floquet Hamiltonian,

$$\hat{\mathcal{H}}_f(t)\phi(t) = \epsilon^{QE}\phi(t), \tag{2.2}$$

where,

$$\hat{\mathcal{H}}_f = \hat{H} - i\hbar\frac{\partial}{\partial t}.$$

Since the Floquet vector is periodic in time, substitution of Fourier expansion of Floquet vector

$$\phi = \sum \phi_n \exp(-in\omega t), \tag{2.3}$$

in equation 2.2 followed by integration over space and one period of time leads to the following transformed expression of $\hat{H}_f$ as derived by Chu [7] :

$$(\hat{H}_f)_{\alpha n,\beta m} = \left[\frac{\hat{P}^2}{2M} + U_{\alpha,\beta}(R) + n\hbar\omega\right]\delta_{\alpha\beta}\delta_{nm} + \left[\frac{1}{2}\mu_{\alpha\beta}(R).\epsilon_0\right]\delta_{(n,m=n\pm1)}\cdot(1-\delta_{\alpha\beta}), \tag{2.4}$$

where α and β denotes the electronic states and index m and n goes over the Fourier expansion of Floquet vector ranging from $+\infty$ to $-\infty$.

To describe both, the ground $(1s\sigma_g)$ and the first excited repulsive $(2p\sigma_u)$ electronic states, we use the following Morse potential [7]:

$$U_i(R) = D_0\left(\exp\left[-2\alpha(R-R_e)\right] - 2t_i\exp\left[-\alpha(R-R_e)\right]\right), (i=1,2) \tag{2.5}$$

We adopt the following expression for the transition dipole moment [7]:

$$\mu_{12}(R) = \mu(R_e) + \frac{\mu'(R_e)}{\alpha y}\left(1-\exp\left[-\alpha y(R-R_e)\right]\right) \tag{2.6}$$

Table 2.1: Molecular parameters for $U_i(R)$ and $\mu_{12}(R)$

potential	$D_0(eV)$	$\alpha(a_0^{-1})$	$R_e(a_0)$	t
$U_1(R)$	2.7925	0.72	2.0	1.0
$U_2(R)$	2.7925	0.72	2.0	-1.11
Trans dipole moment	$\mu(R_e)$	$\mu\prime(R_e)$	y	
$\mu_{12}(R)$	$1.07ea_0$	0.396e	-0.055	

where $\mu'(R_e)$ is the dipole derivative and y is the electronic anharmonicity. The molecular parameters used for $U_i(R)$ and $\mu_{12}(R)$ are listed in Table 2.1 [4].

The laser molecular interaction, described in equation 2.6, is in the length form. This dipolar interaction can also be expressed in terms of velocity form:

$$V^v_{\alpha\beta}(R) = -(e/mc)A \cdot \langle \chi_\alpha(r,R)|P|\chi_\beta(r,R)\rangle \tag{2.7}$$

where A is the vector potential ($A = c/\omega\epsilon_0$) and P is the electronic momentum operator. The dipolar interaction in the velocity form is related to that in the length form via the following relation:

$$V^v_{\alpha\beta}(R) = i\left[(U_\alpha(R) - U_\beta(R))/\hbar\omega\right] V^L_{\alpha\beta}(R) \tag{2.8}$$

where $V^L_{\alpha\beta}(R) = -\mu_{\alpha\beta}(R)\cdot\epsilon_0$ is the electric-dipole coupling in the length form. Here we present the results using velocity form. It is convenient to use the velocity form as the potential coupling term vanishes asymptotically. For implementation of the SES, $\hat{V}_{CAP}$ needs to be added to the kinetic energy term. The Hamiltonian takes the following form:

$$\begin{aligned}(\hat{H}_f)_{\alpha n,\beta m} = &\left[\frac{\hat{P}^2}{2M} + U_{\alpha,\beta}(R) + n\hbar\omega + \hat{V}_{CAP}\right]\delta_{\alpha\beta}\delta_{nm} \\ &+ \left[\frac{1}{2}\mu_{\alpha\beta}(R).\epsilon_0\right]\delta_{(n,m=n\pm1)}\cdot(1-\delta_{\alpha\beta}),\end{aligned} \tag{2.9}$$

The differentials in V_{CAP} in equation 2.9 are calculated analytically and integration is carried out numerically for the matrix representations of V_{CAP}. The matrix elements

of V_{CAP} are complex symmetric. Representation of the remaining part of $(\hat{H}_f)_{\alpha n,\beta m}$ is Hermitian. That is why the total representation becomes complex general. The resonances are calculated by diagonalizing this Hamiltonian. A LAPACK subroutine for general complex matrix diagonalization is used. The real part (E_r) of the eigenvalue provides the position of the resonances and inverse of the imaginary part (Γ) is proportional to the life time of the resonances. Using the SES method, we have computed the complex quasi-vibrational energies of H_2^+ for wavelength (Λ)=2660 Å . Some of the results are presented in the next section.

2.2 Results and discussion

The Floquet electronic-field potential curve crossings are shown in Fig. 2.1. Here each Floquet channel $\mid g,n\rangle$ and $\mid e,n\rangle$ represent ground electronic ($1s\sigma_g$) and first excited electronic state ($2p\sigma_u$) potential surface respectively dressed by "n" photons. $\mid g,0\rangle$ and $\mid e,-1\rangle$ forms a single Floquet block. In Fig. 2.1, potential corresponding to three Floquet blocks are shown i.e. one Floquet block moved by 2ω is added to either side of $\mid g,0\rangle$ and $\mid e,-1\rangle$ block [7]. Black broken and solid lines represent the diabatic potential curve. Coloured solid lines represent the adiabatic potential curve for laser field amplitudes of $0.02, 0.03$ and 0.04 a.u. respectively.

In Fig. 2.2, positions of resonances [Re (E)] vs. width of resonances [Im (E)] for laser field amplitude of 0.001 a.u. have been plotted. Here, convergence of the results with respect to different SES parameters (i.e., λ, x_0 and θ) and complex paths are checked. The continuum states rotate differently with respect to scaling parameters and complex paths. But the resonance states are invariant. In Fig. 2.2 (a), SES results for different complex paths [9, 25] are presented. Plot of g(x) for different complex paths used in Fig. 2.2 (a) are given in Fig. 2.3. In Fig. 2.2 (b) and 2 (c), SES results for x_0=12 and 13 a.u. and λ=0.4 and 0.5 a.u. are plotted respectively. SES results for θ=0.08 and 0.09 radian are plotted in Fig. 2.2 (d). SES results for different number

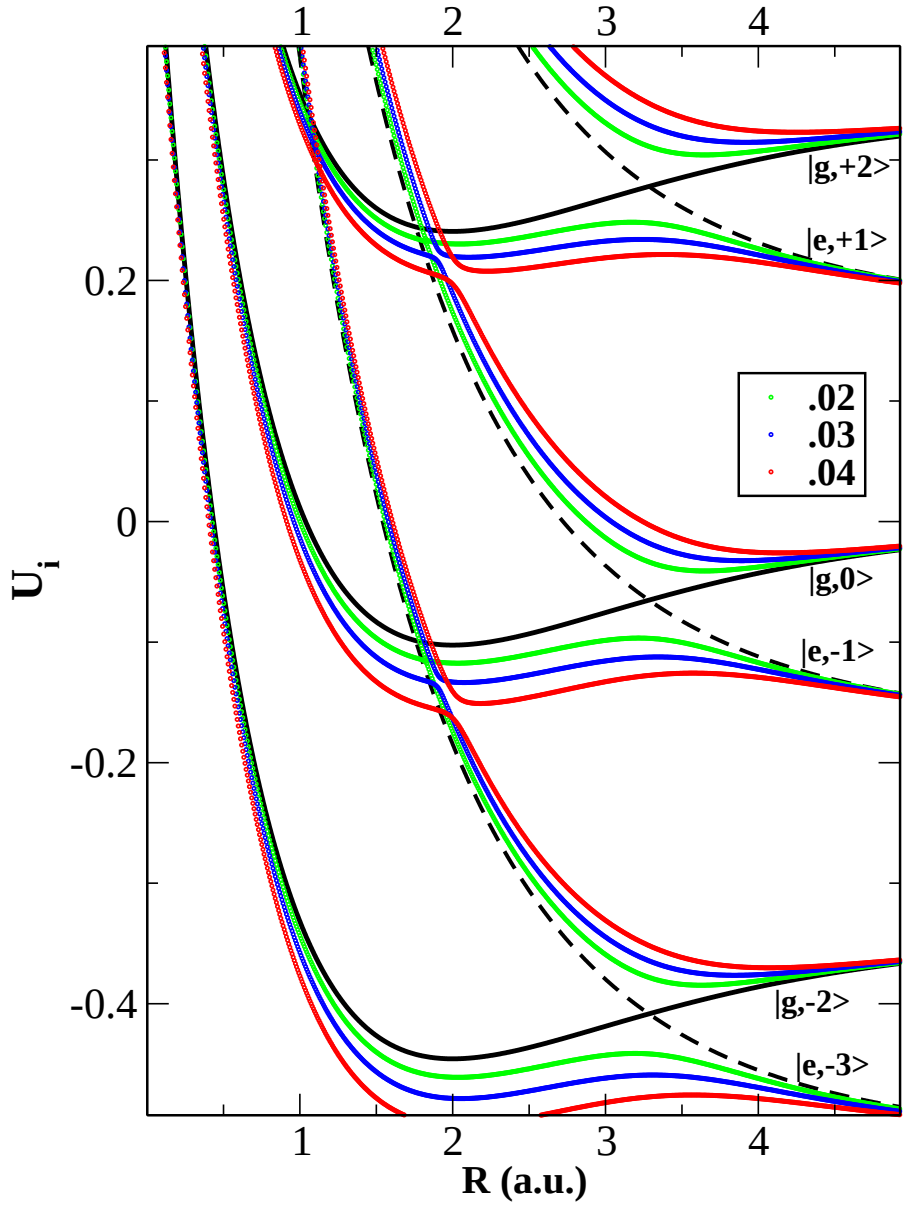

Figure 2.1: Diabatic (black line) and adiabatic (coloured line) potential-energy curves for the two electronic states of H_2^+ dressed by n=0, -1, -2, -3 photons of wave length 2660 Å and laser field amplitudes of 0.02, 0.03 and 0.04 a.u.

of basis functions are given in Fig. 2.2 (e). Here,results corresponding to 100, 150 and 350 basis functions are given. It has been found that results obtained from 150 and 350 basis functions have no observable difference. Hence, we can conclude that for convergence, the minimum number of basis functions required is 150. The unscaled potential is used for Fig. 2.2 (a) to 2.2 (e). In Fig. 2.2 (f), SES results for the scaled and unscaled potential are plotted. From the Fig. 2.2, it is clear that resonances are invariant with respect to the different SES parameters, different complex paths, scaled and unscaled potential.

In Fig. 2.4, we have plotted Re (E) (a.u.) vs. $\Gamma/2$ (a.u.) obtained from SES where potential is scaled, unscaled and complex scaled [7] for different laser field amplitudes ranging from 0.001 a.u to 0.04 a.u at an interval of 0.001 a.u. Here, first (ν=0), second (ν=1) and third (ν=2) resonance states are pointed by the arrows at laser field amplitude of 0.001 a.u. It is evident from the plot that there is no noticeable difference in results. In case of scaled potential and for laser field amplitude of 0.01 a.u., increase in number of basis functions (>350), leads to the convergence of the results up to seven significant figures. In case of lower field amplitudes, results are even better. When the potential is not scaled, SES results follow the qualitative trend for the complete range of amplitudes and the vibrational quantum numbers i.e. ν=1, 2, 3,....etc. For laser field amplitude of 0.001 a.u., unscaled SES results converge up to five significant figures as compared to the scaled SES results. From hereon, all calculations are carried out with the scaled potential and 350 basis functions.

In Fig. 2.5, we have plotted the resonance width or $\Gamma/2$ vs. laser field amplitudes when different number of Floquet blocks are included in the simulation. In the top left panel, we plot the decay of first resonance state (ν=0) when one Floquet block is included for SES and CS. In the bottom left panel, we plot the decay of first resonance state when five and seven Floquet blocks are included. It is clear from this figure that the calculation is convergent with respect to number of Floquet blocks. From hereon, all the results provided are calculated by using five Floquet blocks. It is evident from

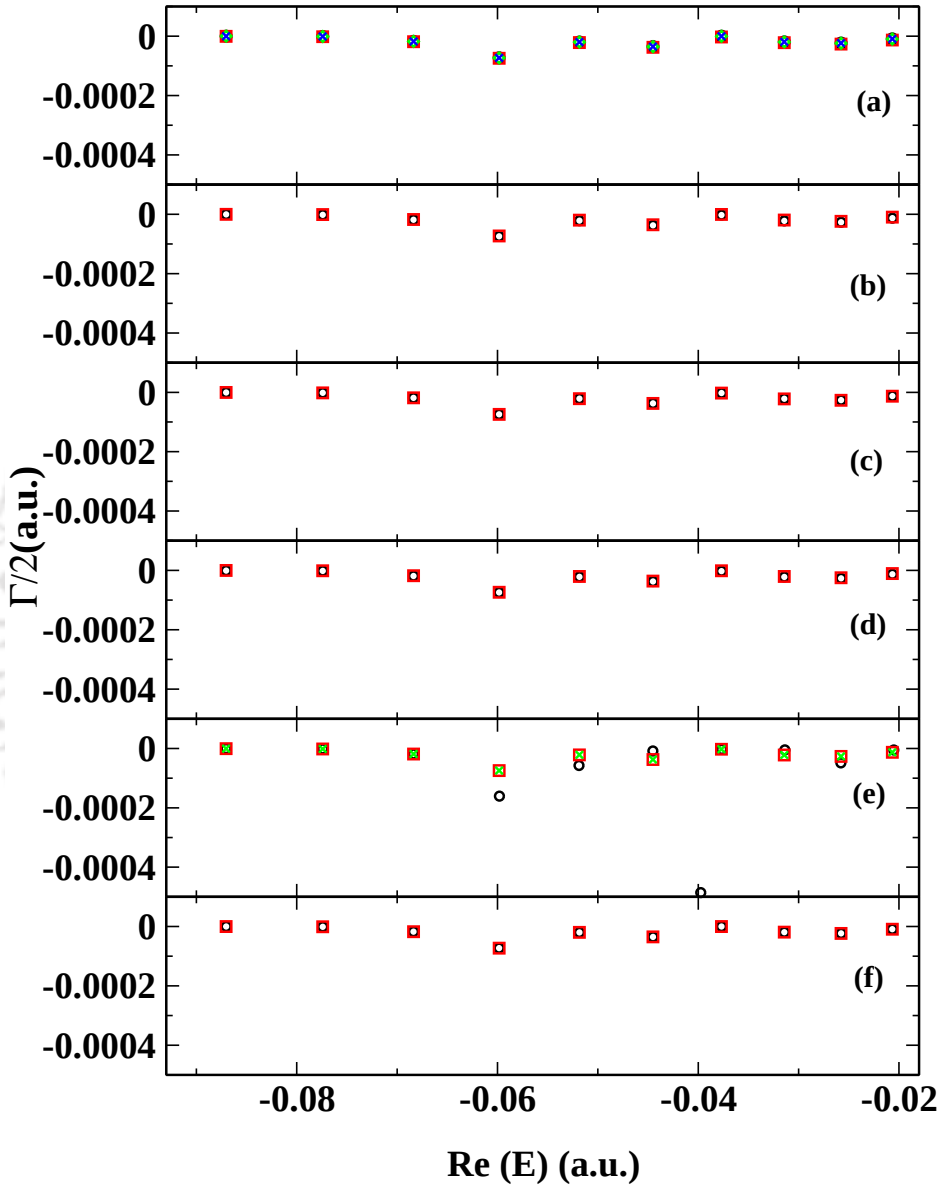

Figure 2.2: Plot of positions of resonances [Re (E)] vs. width of resonances [Im (E)] for laser field amplitude of 0.001 a.u. SES results for Moiseyev path [63](represented by circles), Wood-Saxon path [25](represented by squares), Taylor path [25](represented by diamonds) & Elander path [9](represented by crosses) in Fig. 2.2 (a); λ=0.4 (circles) & λ=0.5 (squares) in Fig. 2.2 (b); θ=0.08 (circles) & θ=0.09 (squares) in Fig. 2.2 (c); x_0=12 (circles) & x_0=13 (squares) in Fig. 2.2 (d); 100 basis functions (circles), 150 (squares) & 350 (crosses) in Fig. 2.2 (e) and scaled (squares) and unscaled potential (circles) in Fig. 2.2 (f) are plotted.

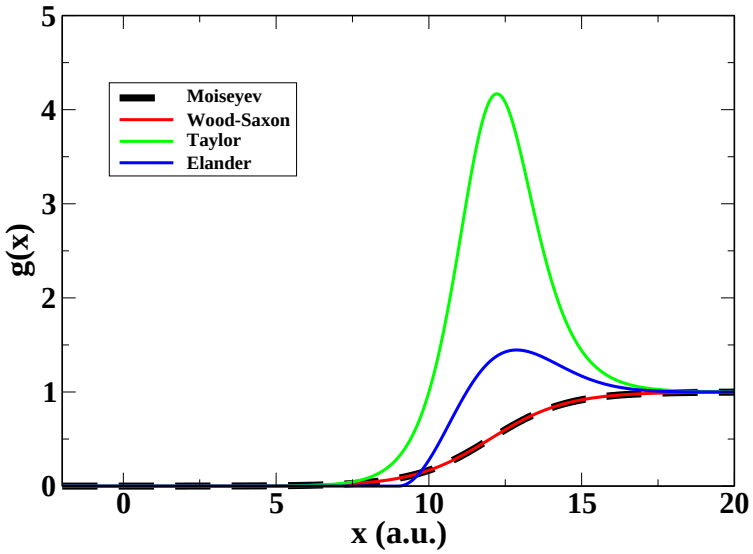

Figure 2.3: Plot of g(x) (used in Fig. 2.2 (f)) vs. X.

the figure that the dissociation rate of the first resonance state is of many orders higher, if more than one Floquet blocks are included in the calculation. Even at lower field amplitude (10^{11} W/cm^2), multiphoton transitions play a dominant role in the photodissociation process. In the top and bottom right panel, we plot decay of third resonance state (ν=2) when one, five or seven Floquet blocks are included. It is interesting to observe that the width ($\Gamma/2$) of third resonance state starts decreasing around the field amplitude of $\sim$ 0.022 a.u.

In Fig. 2.6 and Fig. 2.7, the wavefunctions of first and third resonance states corresponding to $\mid g, 0\rangle$, $\mid e, -1\rangle$, $\mid g, -2\rangle$, and $\mid e, -3\rangle$ Floquet channels have been plotted for different field amplitudes. From this figure, it is evident that for the first resonance state, $\mid g, -2\rangle$ channel is primarily responsible for the photodissociation. Similar results are also observed for field amplitudes of $0.001, 0.002$, a.u. and so on. From these figures, we can conclude that the photodissociation of H_2^+ is a three-photon absorption followed by one-photon stimulated emission, even at lower field amplitudes i.e. at $0.001, 0.002$ a.u. and so on. No one-photon dissociation takes place

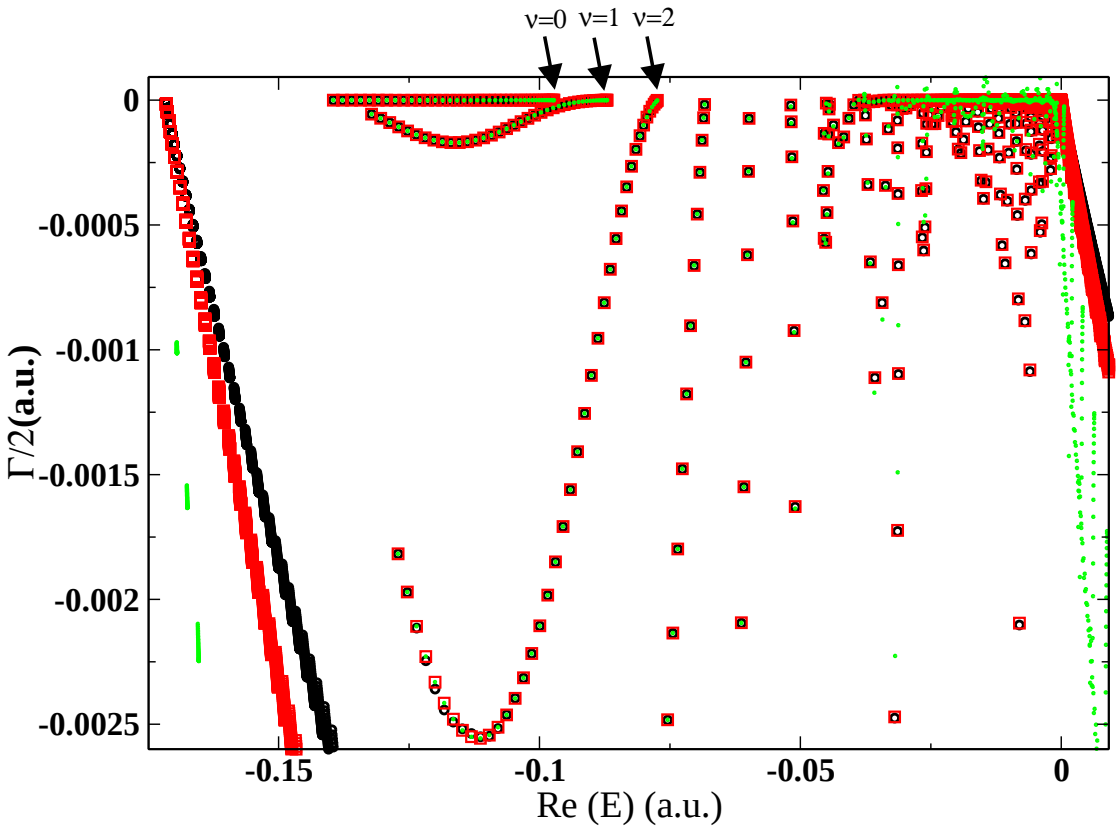

Figure 2.4: Plot of positions of resonances [Re (E)] vs. width of resonances [Im (E)] for different laser field amplitudes ranging from 0.001 a.u. to 0.04 a.u. at an interval of 0.001 a.u. Here squares, circles and dots represent SES results (potential scaled), SES results (potential unscaled) and CS results [7] respectively. Arrows point to the first three resonances at laser field amplitude of 0.001 a.u. Resonances follow a smooth curve as the field amplitudes changes.

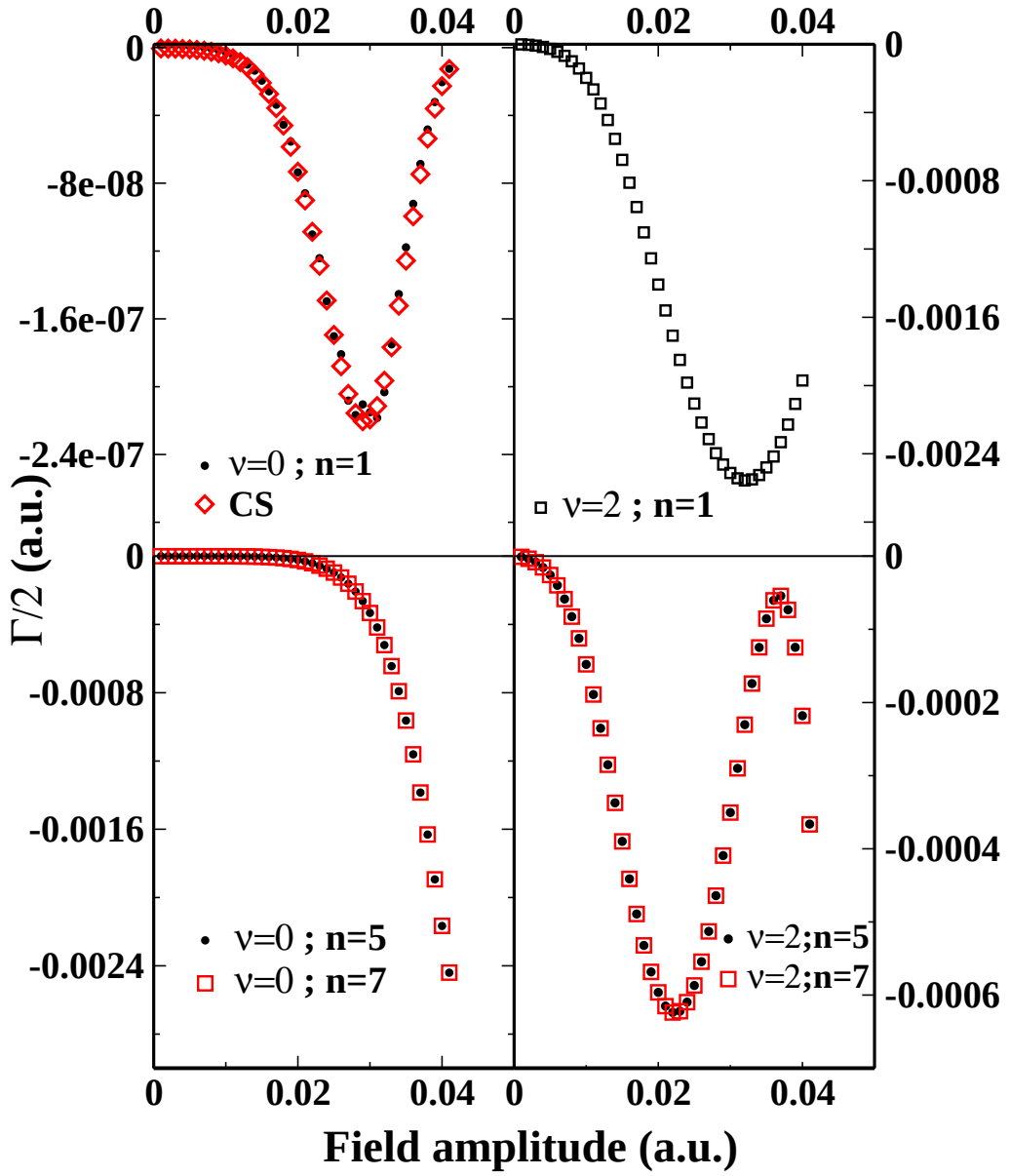

Figure 2.5: Plot of resonance width ($\Gamma/2$) vs. laser field amplitude for first (ν=0) and third resonance states (ν=2) with different number of Floquet blocks (n). In the top panel only one photon transition is included and in the bottom panel up to 5 and 7 (n=5 and 7 respectively) photons transitions are included.

for the first resonance state at intensities ranging from 10^{10} to 10^{14} W/cm^2. The wavefunctions on channel $\mid g, 0\rangle$ possess the nodal structure like a bound state of field free $\mid g, 0\rangle$ potential. For this reason, the first and third resonance states are denoted as ν=0 and 2 respectively i.e. vibrational states of field free $\mid g, 0\rangle$ channel. It is evident from Fig. 2.7 that for the third resonance state, initially photodissociation takes place from $\mid e, -1\rangle$ channel. But around field amplitude of 0.022 a.u., the wavefunction starts decreasing from $\mid e, -1\rangle$ channel and at the same time, continuum tail in $\mid g, -2\rangle$ channel starts increasing. Hence, at high intensities, dissociation takes place from mainly $\mid g, -2\rangle$ channel. This is the reason for the decrease of $\Gamma/2$ for the third resonance state around field amplitude of 0.022 a.u.

In case of third resonance, with the increase in field amplitude (i.e. up to ~ 0.022 a.u.), $\Gamma/2$ first increases. With the further increase in amplitude, $\Gamma/2$ decreases. This phenomenon can also be explained from the dressed picture given in Fig. 2.1. With the increase in amplitude, the adiabatic potential gets lowered. So real part of the energy decreases (as shown in Fig. 2.8) for the first and third resonance state. The barrier at one-photon crossing is also getting lowered with the increase in amplitude. The barrier heights at field amplitudes of 0.02, 0.03 and 0.04 a.u. are -0.0967, -0.1124 and -0.1257 a.u. respectively. At the field amplitude of 0.022 a.u., the real part of the energy i.e. the position of the third resonance state becomes lower than the barrier height and as a result photodissociation from $\mid e, -1\rangle$ channel is discouraged and photodissociation from channel $\mid g, -2\rangle$ becomes dominant.

In Fig. 2.9, Re (E) (a.u.) vs. $\Gamma/2$ (a.u.) for laser field amplitudes 0.006 and 0.02 a.u. has been plotted. From this figure, it is observed that for higher laser field amplitude i.e. 0.02 a.u., new states start appearing indicated in the figure by the arrow. These states have nearly zero width (Γ) or infinite life time. We have plotted the wavefunctions for the first two such states on $\mid g, 0\rangle$ and $\mid e, -1\rangle$ channels in Fig. 2.10. These states are localized around one-photon crossing. They possess well defined nodal structure like bound states. Wavefunctions of these states in other

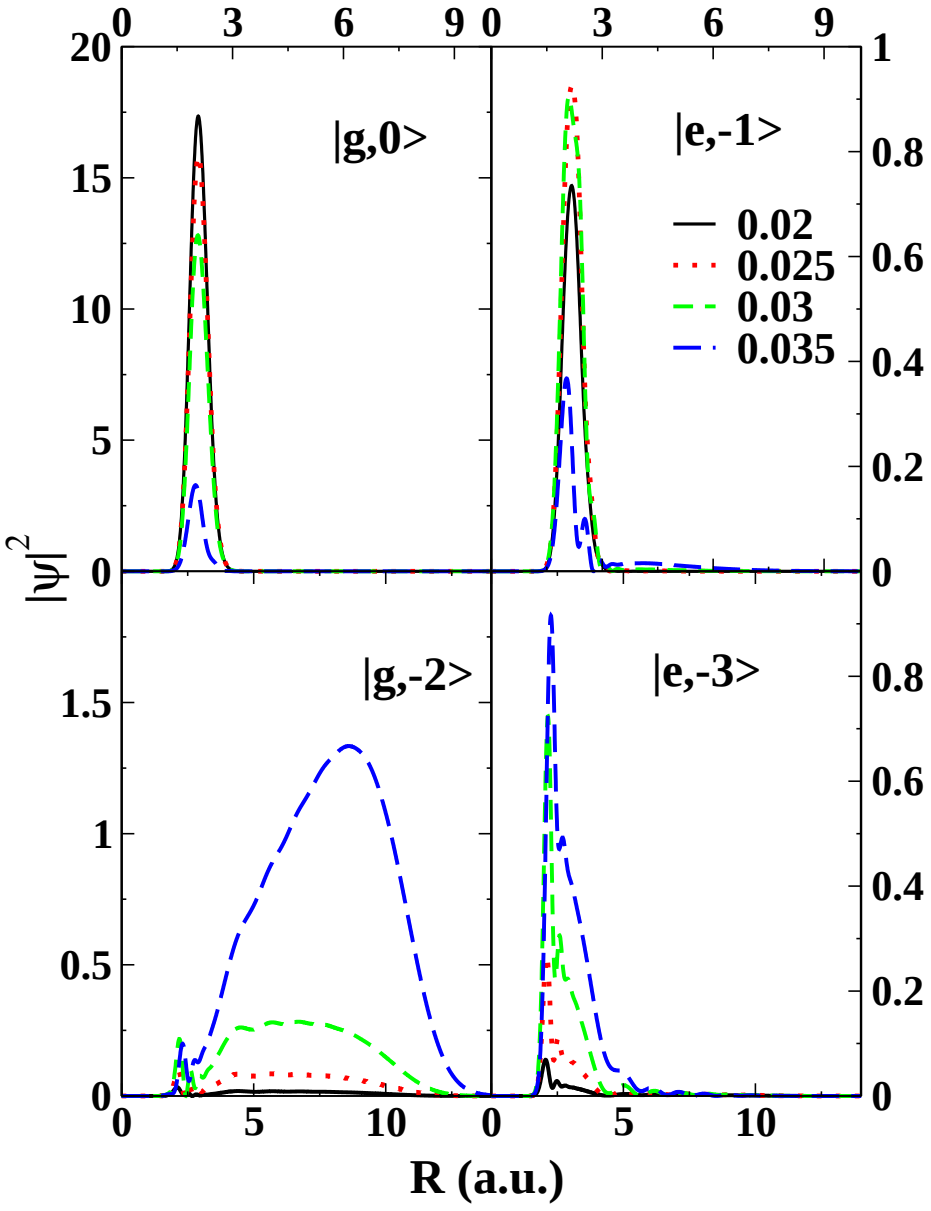

Figure 2.6: Plot of unnormalized $|\psi|^2$ vs. R of first resonance for different laser field amplitudes on different Floquet channels (see Fig. 2.1).

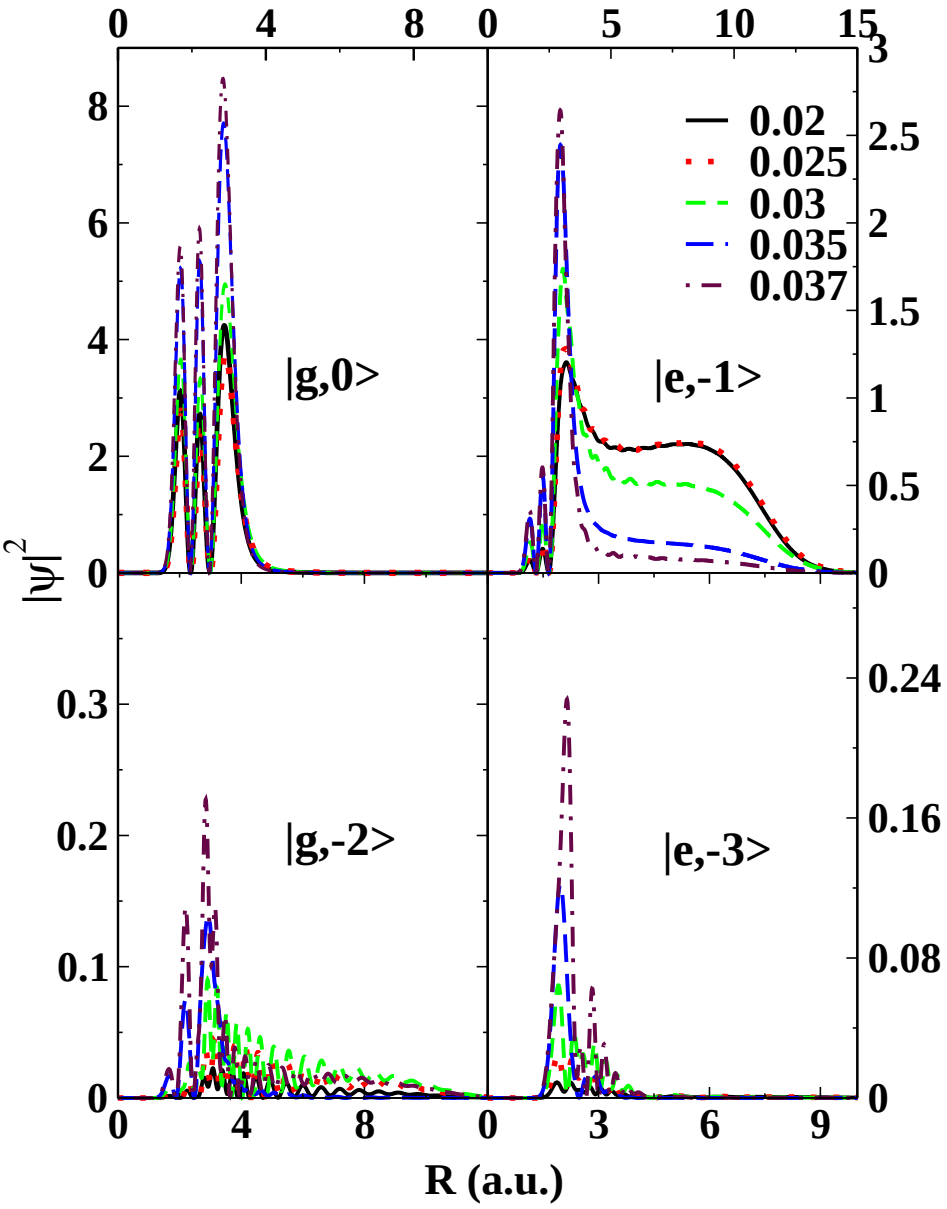

Figure 2.7: Plot of unnormalized $|\psi|^2$ vs. R of third resonance for different laser field amplitudes on different Floquet channels (see Fig. 2.1).

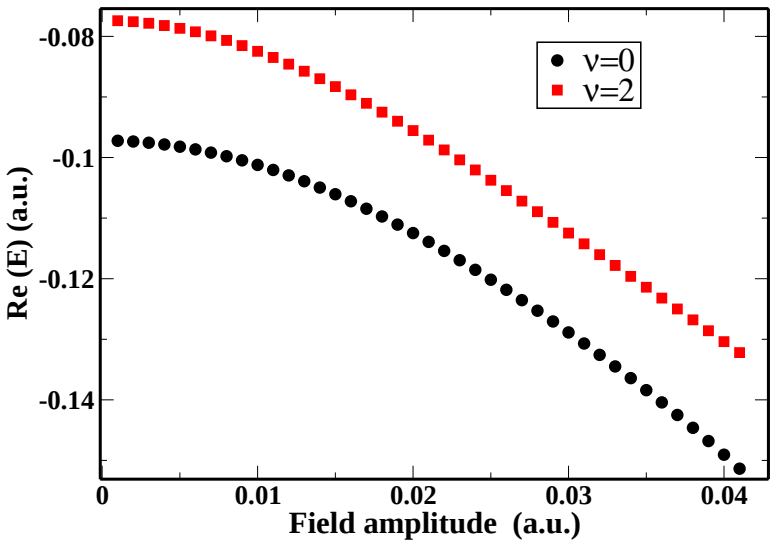

Figure 2.8: Plot of Real part of resonance energy i.e. resonance positions as a function of laser field amplitudes for first (ν=0) and third resonance states (ν=2).

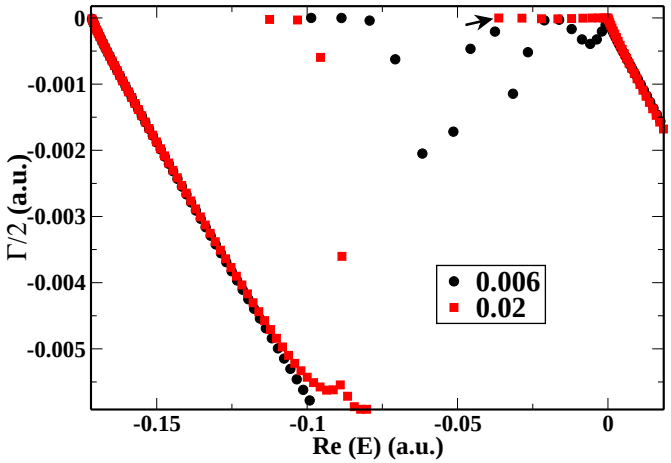

Figure 2.9: Plot of positions of resonances [Re (E)] vs. width of resonances [Im (E)] for laser field amplitudes of 0.006 and 0.02 a.u. Note the appearance of states having nearly zero width (bound states) for laser field amplitudes of 0.02 a.u. shown by arrow.

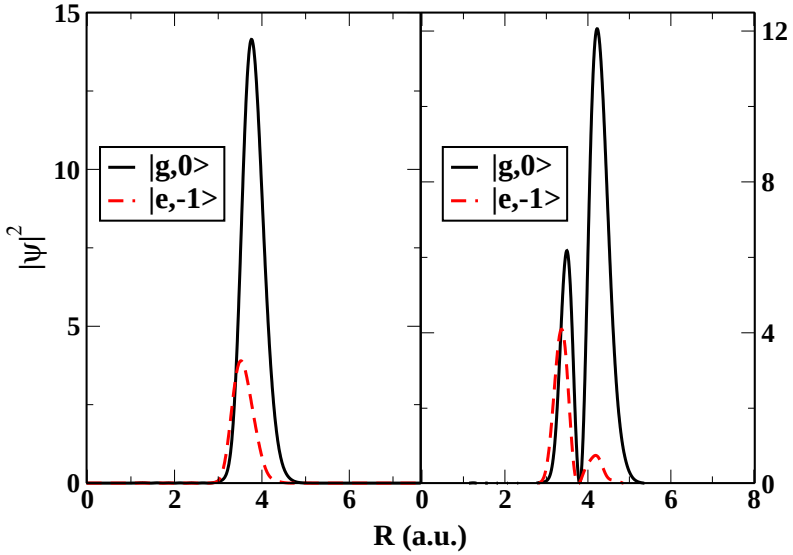

Figure 2.10: Plot of unnormalized $|\psi|^2$ vs. R of first and second bound states (see Fig. 2.9) for laser field amplitude of 0.02 a.u. These states possess well defined nodal structure and localized over one-photon crossing.

Table 2.2: SES parameters used for calculation of resonance energies

λ	θ	x_0	x_{end}
0.4	0.09	12	20

Floquet channels are nearly zero. These states correspond to vibrationally trapped (bond-hardening) states. In case of lower laser field amplitude i.e. 0.006 a.u., no such states are seen.

2.3 Concluding remarks

A study of multiphoton dissociation of H_2^+ in intense laser field using smooth exterior scaling method to calculate resonance states is presented. This method is very attractive as it doesn't disturb the interaction region. The wavefunctions calculated with this method provide indisputable proof in support of mechanisms for different phenomena happening during photodissociation. Wavefunctions corresponding to the

"vibrationally trapped" (bond-hardening) states are found. An unequivocal mechanism for "bond-softening" is provided. It is observed that with an increase in field amplitude, the life time of low vibrational level increases. The mechanism for this novel phenomenon is also explained. In summary, we have calculated the resonance states of H_2^+ accurately with the help of SES method. It is a first attempt of SES implementation to photodissociation dynamics. The undistorted resonance wavefunctions have been calculated for the first time. No one-photon dissociation takes place from ground vibrational state of H_2^+ at the amplitude range of 10^{10} to 10^{14} W/cm^2. The multiphoton dissociation is dominant route for dissociation even at lower intensities. We have identified the bond-hardening states. Indeed, the vibrational states of ground electronic state of H_2^+ which overlap with these bond-hardening states will survive during photodissociation. Some resonance states become more stable with the increase in intensity due to lowering of the adiabatic potential. We report that the stability of these states is not due to usual vibrational trapping.

Chapter 3

USE OF MODIFIED SMOOTH EXTERIOR SCALING METHOD AS AN ABSORBING POTENTIAL AND ITS APPLICATION

In this Chapter, we have used SES method for the first time in the time-dependent dynamics problem wherein the complex scaling function $\theta(x)$ has spatial dependence and is real rather than complex. The usual implementation of SES begins by choosing a derivative of scaling path [F(x)], which is given by

$$f(x) = \frac{\partial F}{\partial x} = 1 + [exp(i\theta_0) - 1]g(x),$$

where θ_0 is the scaling parameter and g(x) goes smoothly from 0 to 1, resulting in f(x) going smoothly from 1 to $\exp(i\theta_0)$. Instead, we define the scaling path [F(x)] as

$$F(x) = xe^{i\theta(x)} = xe^{i\theta_0 g(x)},$$

where $\theta(x)$ goes smoothly from 0 to θ_0. This implementation accomplishes the scaling in a much smoother way and we will show that this type of scaling gives more efficient absorption of the artificial reflections during wavepacket propagation at the grid boundary. We have calculated resonance energies and width of H_2^+ in an intense laser field undergoing multiphoton dissociation (MPD) using this modified smooth exterior scaling (MSES) method and compared with our previous results (given in **Chapter 2**) [22]. This system has been investigated earlier by Chu and co-workers to calculate the resonance states using complex scaling method (CSM) [7].

3.1 Conventional and Modified smooth exterior complex scaling method (CSES and MSES)

Modified smooth exterior scaling (MSES) is a variant of smooth exterior scaling (SES). Here complex path is chosen in such a way that complex scaling path is followed in asymptotic limit. In this method the complex scaling parameter θ_0 is chosen as real.

The Moiseyev-Hirschfelder generalization [46] of the complex coordinate method associates the resonance poles of the S-matrix, $E = E_r - iE_i$, with the θ_0 independent complex eigen values of $\hat{H}$:

$$\hat{H}\Psi = E\Psi, \tag{3.1}$$

where

$$\hat{H} = \frac{-\hbar^2}{2M}\frac{\partial^2}{\partial z^2} + V(z). \tag{3.2}$$

Here $z = F(x)$ is a path in the complex coordinate plane where

$$z = F(x) \longrightarrow x\exp(i\theta_0) \quad \text{as} \quad x \longrightarrow \infty \tag{3.3}$$

The smooth-exterior-scaling path is defined as [63]

$$f(x) = \frac{\partial F}{\partial x} = 1 + [\exp(i\theta_0) - 1]g(x), \tag{3.4}$$

where $g(x)$ varies from 0 to 1 value around the point x=x_0. When $V(x \geq x_0)$=0, unscaled potential $V(x)$ can be used instead of complex potential $V(z)$. The SES Hamiltonian has been derived in earlier publications [25, 43, 58]. In the usual implementation of the SES method, $g(x)$ can be defined as [42, 43]:

$$g(x) = 1 + 0.5\left[\tanh(\lambda(x - x_0)) - \tanh(\lambda(x + x_0))\right]. \tag{3.5}$$

The path derived from this $g(x)$ (equation 3.5) will be referred as Moiseyev path. From here on, implementation using this form of $g(x)$ will be called as conventional SES method (CSES). In the CSES method, g(x) is usually chosen as real and the scaling function $\theta(x)$ related to path F(x) by:

$$F(x) = xe^{i\theta(x)}, \tag{3.6}$$

resulting in $\theta(x)$ becoming complex. Asymptotically when the potential vanishes, the resonance wavefunction takes the following form:

$$\Psi = e^{ikx}.$$

Under complex scaling $x \to xe^{i\theta}$, Ψ is given by

$$\Psi = e^{ikxe^{i\theta}} = e^{ikx\cos\theta}e^{-kx\sin\theta}.$$

Here the second term in Ψ is responsible to make the wavefunction square integrable. When θ is complex i.e., $\theta = \theta_r + i\theta_{im}$, as in the case of CSES, the wavefunction takes

the following form:

$$\Psi = e^{ikxe^{i\theta_r}e^{-\theta_{im}}} = e^{ikx\cos\theta_r e^{-\theta_{im}}} e^{-kx\sin\theta_r e^{-\theta_{im}}},$$

and it is evident that θ_{im} doesn't serve any purpose. Hence, we chose the scaling function $\theta(x)$ as real which makes g(x) complex. The real function $\theta(x)$ is defined as-

$$\theta(x) = a(x)\theta_0 = \theta, \tag{3.7}$$

where a(x) has the following form:

$$a(x) = 1 + 0.5\left[\tanh(\lambda(x - x_0)) - \tanh(\lambda(x + x_0))\right], \tag{3.8}$$

a(x) varies from 0 to 1 around the point x=x_0 and θ_0 is the scaling parameter. After taking first derivative of F(x) (equation 3.6), we have,

$$f(x) = \frac{\partial F}{\partial x} = e^{i\theta} + ixe^{i\theta}\frac{\partial \theta}{\partial x}. \tag{3.9}$$

By comparing equation 3.9 and 3.4, we get

$$g(x) = \frac{e^{i\theta} - 1}{e^{i\theta_0} - 1} + ix\frac{e^{i\theta}}{e^{i\theta_0} - 1}\theta_0\frac{\partial a(x)}{\partial x}. \tag{3.10}$$

Differentiating a(x) with respect to x in equation 3.8 we get the form of g(x) as:

$$g(x) = \frac{e^{i\theta} - 1}{e^{i\theta_0} - 1} + 0.5ix\frac{e^{i\theta}}{e^{i\theta_0} - 1}\theta_0\lambda\left[\cosh^{-2}(\lambda(x - x_0)) - \cosh^{-2}(\lambda(x + x_0))\right] \tag{3.11}$$

From here on, the method having this g(x) (equation 3.11) will be called as modified SES method (MSES). For both the CSES and MSES methods, the complex paths F(x) have been plotted in Fig. 3.1. The scaling parameters i.e., θ_0=0.32, λ=0.28 a.u. and x_0=360 a.u. are used for the both complex paths.

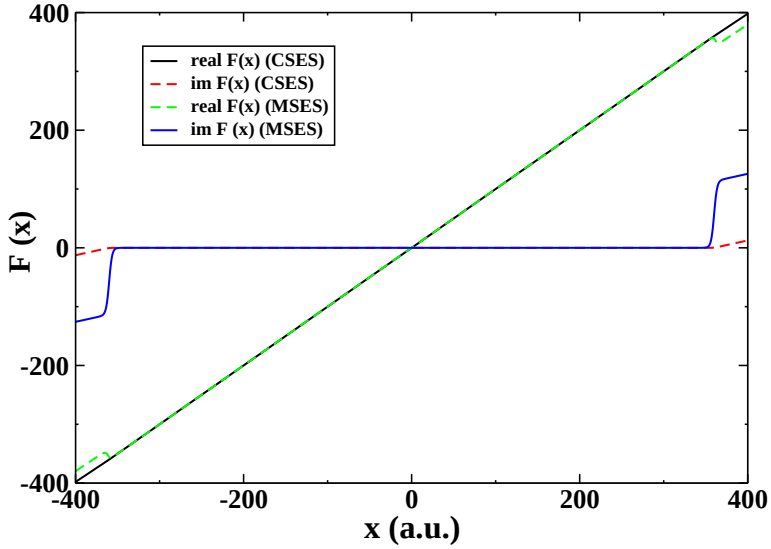

Figure 3.1: Plot of F(x) vs. x.

3.2 Calculation of the wavepacket absorption at the grid boundary

Here we consider a Gaussian wavepacket that moves freely in 1D space [11, 25, 78]. The initial wavepacket is chosen as-

$$\Psi(x, t=0) = \left(\frac{1}{\pi\delta^2}\right)^{1/4} \exp\left(\frac{-(x-x_i)^2}{2\delta^2} + ik_0x\right). \tag{3.12}$$

Where δ=30.0 a_0, x_i=0 a_0 and reduced mass μ=1 [78]. We consider that $\Psi(x)$ is confined in a box initially. With the advancement of time, $\Psi(x)$ with an initial positive momentum $\hbar k_0$, gets out of the box. The analytical solution for the Gaussian free

particle [73] is as follows:

$$\Psi(x,t) = \left(\frac{1}{\pi\delta^2}\right)^{1/4} \exp\left(-\frac{\left(x - x_i - \frac{\hbar k_0 t}{\mu}\right)^2}{\left(2\delta^2 + \frac{2i\hbar t}{\mu}\right)} + ik_0\left(x - \frac{\hbar k_0 t}{\mu}\right) + \frac{i}{\hbar}\left[\frac{(\hbar k_0)^2 t}{2\mu} + \frac{i\hbar}{2}\ln\left(1 + \frac{i\hbar t}{\mu\delta^2}\right)\right]\right) \tag{3.13}$$

The center of the wavepacket is moving with a velocity $\frac{\hbar k_0}{\mu}$. This means that value of $|\Psi(x,t)|^2$, for sufficient large time, becomes negligible within the box. But when numerical calculations are carried out, this is not the precise scenario as the artificial reflections from the edges of the grid are obtained. To avoid these artificial reflections, we need to apply the CSES or the MSES to the Hamiltonian.

The propagation of the wavepacket is carried out with the help of Taylor series expansion method. The short time propagator e^{-iHt} is expanded with the help of Taylor series. Large number of terms are included in the Taylor series to ensure convergence to the 16^{th} digit of each and every term of the propagator matrix . Time step is taken as 0.1 a.u. and the propagation is done for 10^5 time steps. The effectiveness of absorbing potentials is measured by 'Error' calculation [78]:

$$Error = \int_{A_{unscaled}} dx|\Psi_{NUM}(x,T) - \Psi_{Exact}(x,T)|^2 \tag{3.14}$$

Here, $A_{unscaled}$ stands for the unscaled region in space and t=T is the time when $|\Psi(x,t)|^2$ is negligible within the unscaled region.

3.3 Results and discussion

In Fig. 3.2, the error calculation as a function of average momentum of particle (k_0) using the CSES method and the MSES method for box length (L)=800 and 1000 a.u. have been plotted. Plus signs and filled circles represent the error obtained from using the MSES method for L=800 and 1000 a.u. respectively. The grid is divided into 2000

number of grid points. Hamiltonian is prepared in the sinc-DVR representation [8]. The SES terms are included by pre and post multiplication of the kinetic energy matrix by the complex diagonal matrix as shown by Karlsson [25]. Asterisks and filled squares represent the error obtained from using the CSES method for L=800 and 1000 a.u. respectively. For all the four plots, the same scaling parameters i.e., λ=0.28, θ_0=0.32 and x_0=360 a.u. are used. The same parameters were used by Zavin and co-workers [78]. They obtain these parameters after minimizing the error for the CSES method for E=0.01 a.u. which is equal to k_0=0.141 a.u. We have not done any optimization. It is clear from the figure that for the lower k_0 values, the MSES method is better by at least seven orders of magnitude. Moreover, as the scaled region is decreased i.e., grid is reduced from 1000 to 800 a.u. (keeping the other scaling parameters same e.g. x_0=360 a.u.), the CSES results deteriorate by five orders of magnitude while the MSES results remain mostly unchanged. This implies that the MSES method is much more robust with respect to the available grid for scaling. The MSES method thus, will require much lesser grid points for scaling to get accurate results.

We have considered smaller values of k_0. This is due to the fact that for larger k_0 values, absorption of the wavepacket is always excellent in both the MSES and the CSES methods. In fact, the results for large k_0 converge to computer accuracy. However, it is difficult to absorb the artificial reflections from the end of the grid in case of wavepacket having lower k_0 values. This is due to the fact that to absorb a wave having wave number k_0, the absorption region should be of the size $\frac{2\pi}{k_0}$.

The superiority of the MSES over the CSES is also evident from the plot of the propagated wavepacket (Fig. 3.3). Here, we have plotted $\Psi(x,t)$ within the unscaled region at different time intervals for k_0=0.20 a.u. The dashed (red) line represents the analytical results given by equation 3.13. The wavefunction obtained from finite grid numerical calculations using the CSES and MSES results, are denoted by green and black solid lines respectively. The scaling parameters are same as those in Fig. 3.2. It

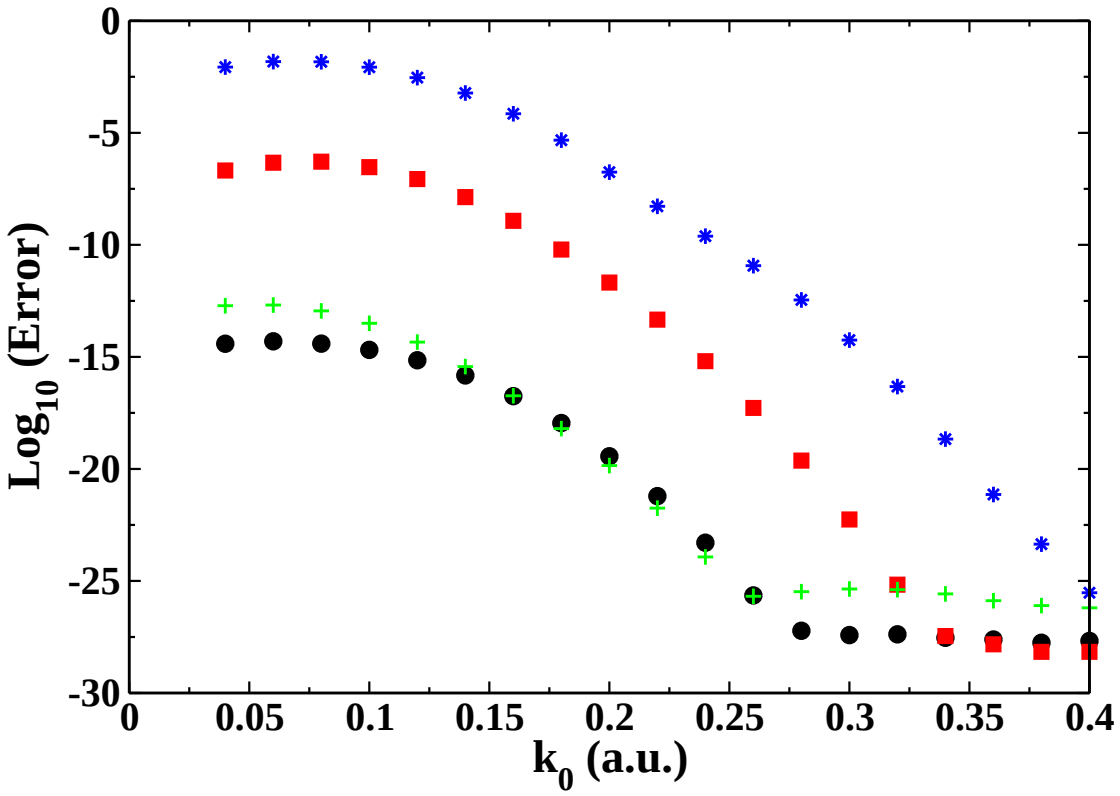

Figure 3.2: Plot of Log_{10} (Error) vs. k_0. The MSES and the CSES results using 1000 grid points are symbolized by circle and square. The MSES and the CSES results using 800 grid points are symbolized by pluses and asterisks.

is evident from the figure that at t=7 $\times 10^3$ a.u., wavefunction calculated using CSES method starts showing wiggles. But the wavefunction calculated using the MSES method matches in value with the analytical result. At t=10^4 a.u., wavefunction calculated using CSES method shows major difference compared to the analytical results. However, wavefunction calculated using the MSES method is still on the top of the analytical wavefunction in the unscaled region.

In Fig. 3.4, we have plotted Log_{10} (Error) as a function of different scaling parameters i.e., x_0, λ and θ_0 for the CSES and MSES methods. We have considered the box length (L)=800 a.u. and the grid has been divided into 2000 number of grid points. In Fig. 3.4 (a), Log_{10} (Error) as a function of x_0 is plotted (where, for MSES λ=0.28 a.u. and θ_0=0.32 and for CSES λ=0.28 a.u. and θ_0=1.30). We have selected high θ_0 for CSES to ensure high accuracy. It is clear from this plot that the results obtained from the MSES method have no dependence on x_0 which implies that the same accuracy can be achieved without using a large grid. CSES needs more space for scaling to get comparable accuracy, which is computationally inefficient. When a large grid is used for scaling i.e., x_0=300 a.u. the MSES results are better by three orders of magnitude compared to that of the CSES results. However, for smaller grid i.e., x_0=380 a.u., the accuracy of the MSES results increases to eleven orders of magnitude compared to that of the CSES results. In Fig. 3.4 (b), Log_{10} (Error) as a function of λ is plotted (where x_0=360 a.u. and θ_0=0.32). It has been clearly seen from this plot that MSES has little dependence on λ whereas CSES is independent. But still accuracy is better in case of MSES results compared to that of the CSES results. In Fig. 3.4 (c), Log_{10} (Error) as a function of θ_0 is plotted (where x_0=360 a.u. and λ=0.28 a.u.). This plot clearly shows a strong dependence of θ_0 on the MSES results compared to that of CSES results. The MSES and CSES results are unstable beyond θ_0=0.33 and 1.50 respectively and not shown beyond those θ_0. But overall, accuracy of the MSES results are many orders of magnitude better than the CSES results. We have applied the SES and the MSES method for calculation of resonances

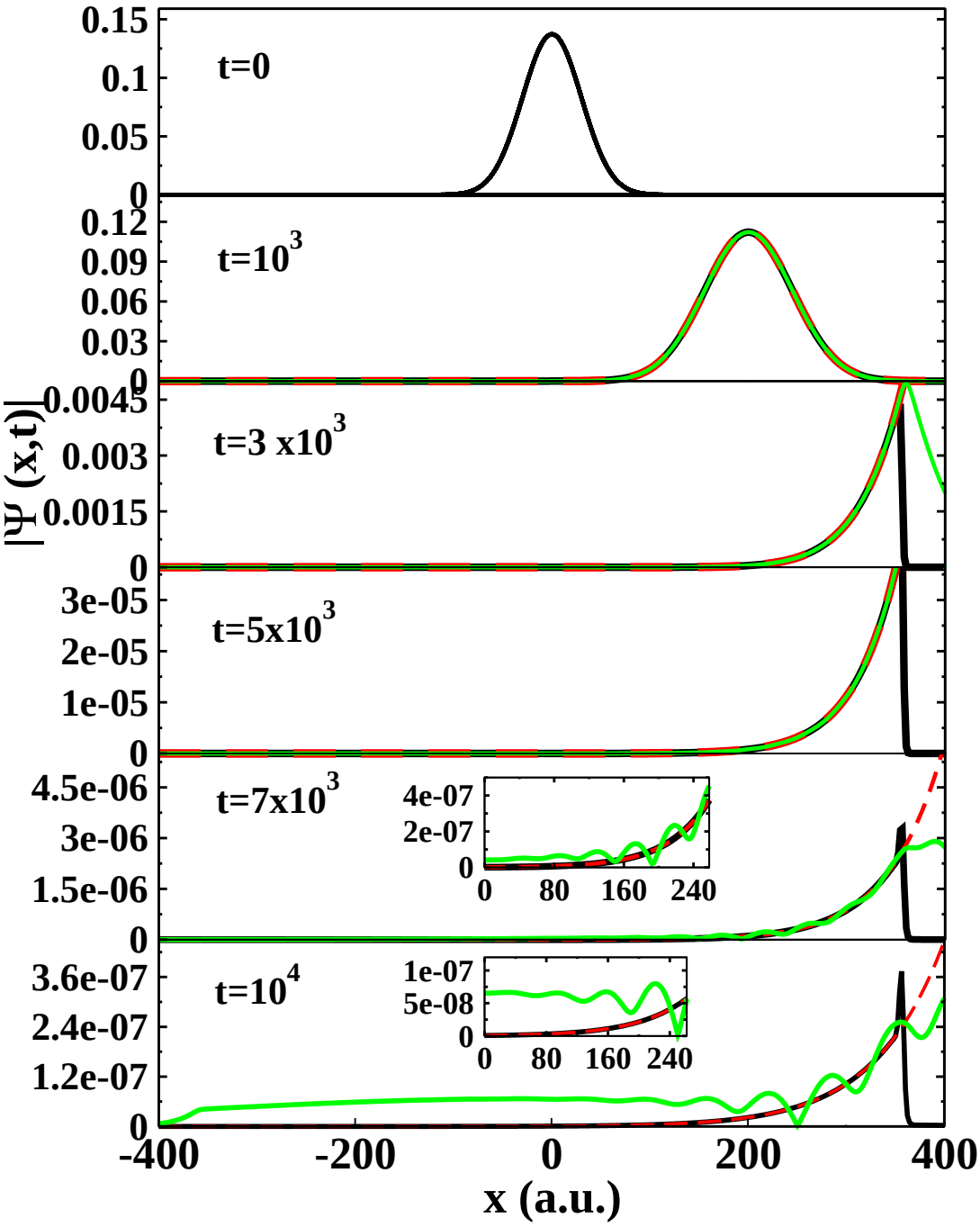

Figure 3.3: Plot of $|\Psi(x,t)|$ vs. x. The exact motion of the wavepacket is denoted by the dashed line (red). The numerical results obtained from the MSES method (black) and the CSES method (green) are denoted by the solid line.

during the photodissociation of H_2^+ molecule. Chu and co-workers [7] had calculated the complex quasienergies by diagonalizing the complex scaled Floquet Hamiltonian whose size in the Fourier Grid basis depends on the number of grid points (N), the number of electronic surfaces involved in photodissociation (m) and the number of photons absorbed (n). The dimension of the Hamiltonian matrix will be $(mN \times mN)$ for a single photon excitation. The form of Floquet Hamiltonian $(\hat{H}_f)$ derived by Chu and co-workers [7] including the SES absorbing term [22] is given by:

$$\begin{aligned}(\hat{H}_f)_{\alpha n,\beta m} = &\left[\frac{\hat{P}^2}{2M} + U_{\alpha,\beta}(R) + n\hbar\omega + \hat{V}_{CAP}\right]\delta_{\alpha\beta}\delta_{nm} \\ &+ \left[\frac{1}{2}\mu_{\alpha\beta}(R).\epsilon_0\right]\delta_{(n,m=n\pm1)}\cdot(1-\delta_{\alpha\beta}),\end{aligned} \tag{3.15}$$

where α and β denote the electronic states and indices m and n go over the Fourier expansion of Floquet vector ranging from $+\infty$ to $-\infty$. Only two electronic states i.e. the ground $(1s\sigma_g)$ and the first excited repulsive $(2p\sigma_u)$ states are considered [7]. We have used Fourier Grid method to represent the Hamiltonian [37]. Kinetic energy operator and SES terms are calculated as shown by Karlsson [25]. The resonances are calculated by diagonalizing this Hamiltonian. A LAPACK subroutine for general complex matrix diagonalization is used. The real part (E_r) of the eigen value provides the position of the resonances and the inverse of its imaginary part (Γ) is proportional to the life time of the resonances. Using the MSES method, we have computed the complex quasi-vibrational energies of H_2^+ for Λ=2660 Å at the field amplitude of 0.005 a.u. We have used 351 basis functions to achieve very high convergence for both E_r and Γ i.e., any more increase in the number of basis functions will not make any perceivable difference to the plots.

We can calculate the resonance states accurately with the help of this new method. A θ-trajectory has been shown for first six resonances calculated from the MSES and the CSES methods [22] in Fig. 3.5, for grid ending at 9 a.u. (x end=9) along with accurate resonance value calculated from the CSM. In this figure, positions of

resonances [Re (E)] vs. width of resonances ($\Gamma/2$) for laser field amplitude of 0.005 a.u., have been plotted. We use the SES parameters x_0=12 a.u. and λ=0.4 a.u. for all the SES calculations shown in this Fig. θ_0 is varied from 0.1 to 2.1 for both the methods. The MSES results and the CSES results for grid ending at 9 a.u. (x end=9 a.u.) are denoted by circles and squares respectively and the accurate CS results are denoted by plus symbol [7, 22]. From this plot, it is seen that MSES results converge toward the accurate CS results. For CS results, we have used 351 number of basis functions and grid ends at 20 a.u. (x end=20 a.u.). First seven resonances calculated by different methods (i.e., from the accurate complex scaling (CS) [7, 22], MSES and CSES methods) are listed in table 3.1 for the easy comparison. We would again like to point out that the value of x_0 is kept equal to 12 a.u. for both the calculations. Results obtained from the CSES method where grid ends at 9 a.u. differ significantly from the other two results (which are indistinguishable). So, we can conclude that the MSES is better than the CSES method for calculation of the resonance states as it requires lesser number of grid points.

3.4 Concluding remarks

Here we propose a new complex path to achieve better absorption during the propagation of a wavepacket. In the proposed modified smooth exterior scaling method, scaling function, $\theta(x)$, has been chosen as a real function rather than complex (as used in a conventional smooth exterior scaling method). It greatly reduces the artificial reflections from the boundary edges. This modified SES method is applied to study the multiphoton dissociation of H_2^+ in intense laser field. The resonance states are calculated accurately. In summary, we have shown that the MSES method is much more efficient in absorbing the wavepacket near the grid boundary than the CSES method. In case of the latter, the accuracy of the results deteriorate as the grid size is decreased. But the modified SES results are mostly unchanged with respect to

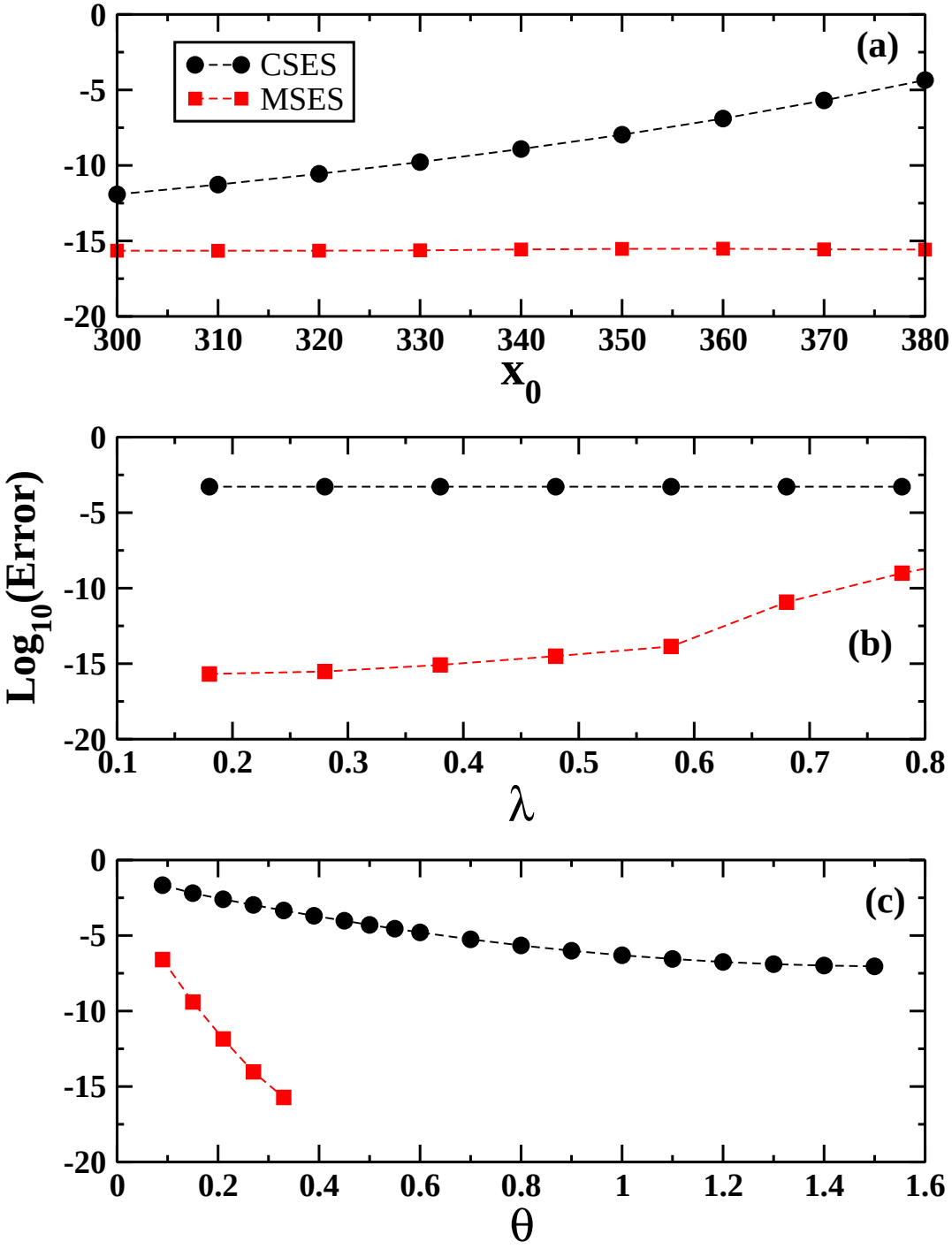

Figure 3.4: Plot of Log_{10} (Error) vs. different scaling parameters for the CSES and MSES methods.

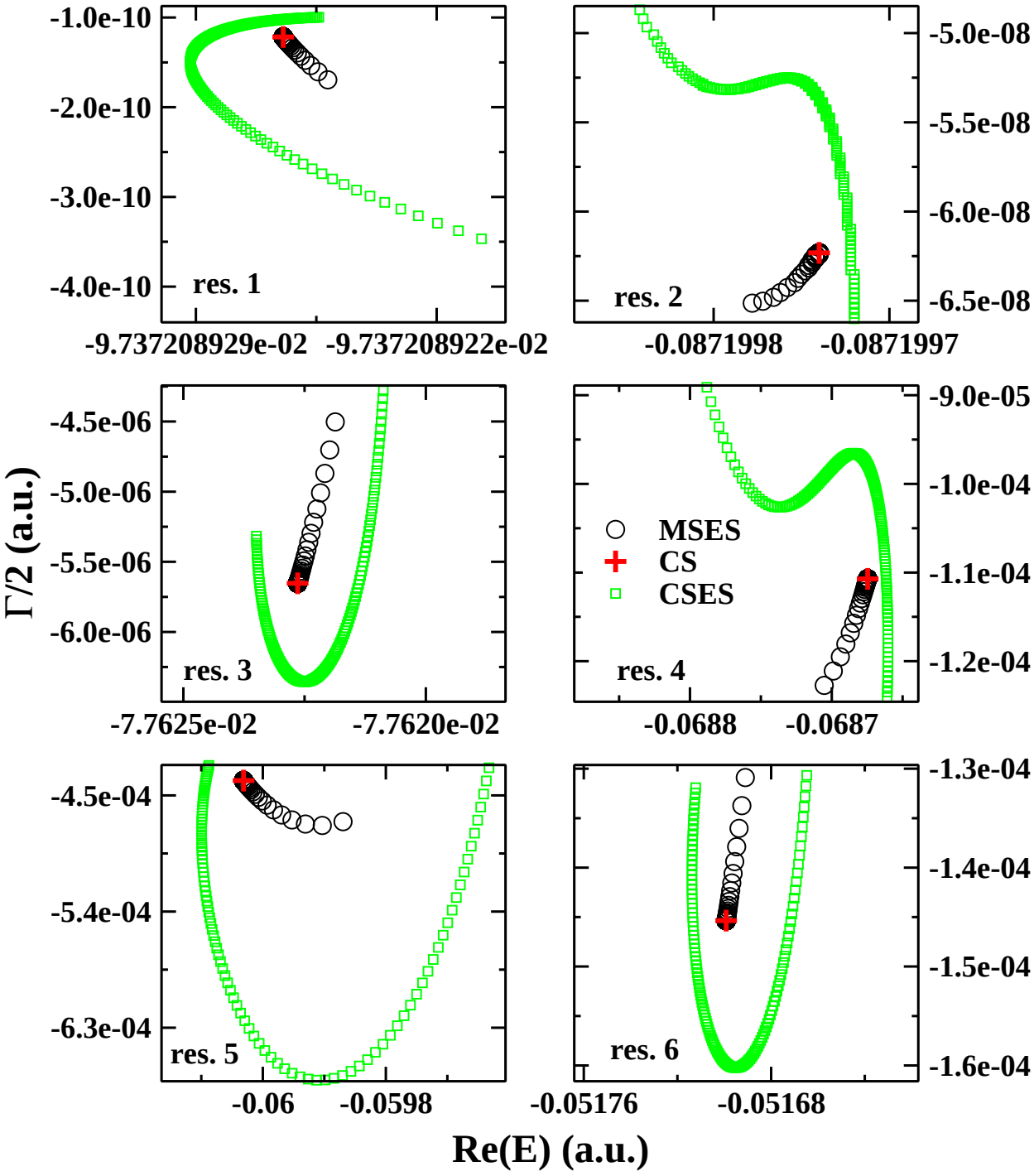

Figure 3.5: Plot of θ-trajectory for first six resonances calculated from the MSES, CSES [22] and accurate complex scaling (CS) methods. Other scaling and grid parameters are kept constant.

Table 3.1: Resonances for the H_2^+ molecule. (A) accurate complex scaling results [7,22]. (B) MSES results (for x end=9 a.u.). (C) CSES results (for x end=9 a.u.) [22]
.

	Real part	Imaginary part
A	-0.0973 7208 9264	-0.0000 0000 0121
B	-0.0973 7208 9264	-0.0000 0000 0121
C	-0.0973 7208 9291	-0.0000 0000 0140
A	-0.0871 9976 9996	-0.0000 0006 2320
B	-0.0871 9976 9996	-0.0000 0006 2320
C	-0.0871 9977 2451	-0.0000 0005 3034
A	-0.0776 2264 2503	-0.0000 0565 2904
B	-0.0776 2264 2503	-0.0000 0565 2904
C	-0.0776 2249 5839	-0.0000 0635 4245
A	-0.0686 7467 1173	-0.0001 1071 9089
B	-0.0686 7467 1173	-0.0001 1071 9089
C	-0.0686 8417 5417	-0.0009 6546 5340
A	-0.0600 3128 6575	-0.0004 3852 0668
B	-0.0600 3128 6575	-0.0004 3852 0668
C	-0.0600 9573 4610	-0.0004 4825 1207
A	-0.0516 9918 8221	-0.0001 4535 4220
B	-0.0516 9918 8221	-0.0001 4535 4220
C	-0.0516 9521 5108	-0.0001 6021 5524
A	-0.0446 2123 2412	-0.0002 0588 9092
B	-0.0446 2123 2412	-0.0002 0588 9092
C	-0.0446 4214 6148	-0.0001 9645 3079

the decreased grid size. We have also calculated different resonance states accurately with the help of the MSES method where θ is real and less number of grid points are required to get the results accurately.

Chapter 4

APPLICATION OF PARAMETRIC EQUATIONS OF MOTION TO STUDY THE LASER INDUCED MULTIPHOTON DISSOCIATION OF H_2^+ IN INTENSE LASER FIELD.

Rabitz and co-workers [38] had put forward a method in which Schrödinger equation was solved explicitly only once and the solutions at other parameter values were obtained by integrating a set of ordinary differential equations through the parameter space of the Hamiltonian. These equations have been termed as parametric equations of motion (PEM). These kind of equations have been applied initially in the field of quantum chaos [54, 76, 77]. Later PEM was implemented by Gross et al. [14, 15] to

obtain the 3-D plots of population dynamics as a function of frequency and phase or amplitude. In their method, time dependent Schrödinger equation (TDSE) was needed to be solved once to obtain the quantum dynamic behaviour in the presence of strong (nonperturbative) periodic fields having the form $A\cos(\omega t)$ over a range of field amplitudes and frequencies. This method utilizes Floquet theory as well and integrates through frequency and amplitude space using PEM for quasienergies and Floquet eigen vectors. The advantage of PEM lies in the fact that one can trace the individual eigen states in parameter space. In this Chapter, we have tried to implement PEM jointly with smooth exterior scaling method (SES) to study the photodissociation dynamics of H_2^+. To the best of our knowledge, this is the first time that PEM has been applied for any photodissociation problem (viz. H_2^+) to calculate resonance states. This is the first application of PEM to non-Hermitian Hamiltonian.

4.1 Floquet formalism for PEM

Chu and co-workers [7] had calculated the complex quasienergies by diagonalizing the complex scaled Floquet Hamiltonian whose size in the Fourier Grid basis depends upon the number of grid points (N), the number of electronic surfaces involved in photodissociation (m) and the number of photons absorbed (n). The dimension of the Hamiltonian matrix will be $(mN \times mN)$ for a single photon excitation. The form of Floquet Hamiltonian $(\hat{H}_f)$ derived by Chu and co-workers [7] including the SES absorbing term (i.e., complex absorbing potential (V_{CAP}) term) [22, 23, 25] is given by:

$$(\hat{H}_f)_{\alpha n,\beta m} = \left[\frac{\hat{P}^2}{2M} + U_{\alpha,\beta}(F(R)) + n\hbar\omega + \hat{V}_{CAP}\right]\delta_{\alpha\beta}\delta_{nm} + \left[\frac{1}{2}\vec{\mu}_{\alpha\beta}(F(R)).\vec{A}_0\right]\delta_{(n,m=n\pm1)}\cdot(1-\delta_{\alpha\beta}), \tag{4.1}$$

where α and β denote the electronic states and indices m and n go over the Fourier expansion of Floquet vector ranging from $+\infty$ to $-\infty$. Here μ is the dipole operator, A_0 and ω are the amplitude and frequency of the laser respectively. Here F(R) is the path in the complex coordinate plane defined as [63]:

$$\frac{\partial F}{\partial R} = 1 + [\exp(i\theta_0) - 1]g(R),$$

where g(R) is varied from 0 to 1 smoothly around the point R=R_0 and θ_0 and λ are the scaling parameters. We have used three different smooth exterior scaling paths: Moiseyev path [22, 42, 43, 46, 63, 64]

$$g(R) = 1 + 0.5\left[\tanh(\lambda(R - R_0)) - \tanh(\lambda(R + R_0))\right], \tag{4.2}$$

$$F(R) = R + (e^{i\theta} - 1)\left[R + \frac{1}{2\lambda}\ln\frac{\cosh[\lambda(R - R_0)]}{\cosh[\lambda(R + R_0)]}\right]. \tag{4.3}$$

Taylor path [22, 25]:

$$\begin{aligned} g(R) = {} & (1 + e^{(R_0 - R)\lambda})^{-1} + (1 + e^{(R_0 + x)\lambda})^{-1} + R\lambda \\ & \left[e^{(R_0 - R)\lambda}(1 + e^{(R_0 - R)\lambda})^{-2} - e^{(R_0 + R)\lambda}(1 + e^{(R_0 + R)\lambda})^{-2})\right], \end{aligned} \tag{4.4}$$

$$F(R) = R + (e^{i\theta} - 1)R\left[(1 + e^{\lambda(R_0 - R)})^{-1} + (1 + e^{\lambda(R_0 + R)})^{-1}\right]. \tag{4.5}$$

Modified smooth exterior scaling (MSES) path [23]:

$$F(R) = Re^{i\theta(R)}, \tag{4.6}$$

where

$$\theta(R) = \left[1 + 0.5(\tanh(\lambda(R - R_0)) - \tanh(\lambda(R + R_0)))\right]\theta_0, \tag{4.7}$$

and

$$g(R) = \frac{e^{i\theta}-1}{e^{i\theta_0}-1} + 0.5iR\frac{e^{i\theta}}{e^{i\theta_0}-1}\theta_0\lambda\left[\cosh^{-2}\left(\lambda(R-R_0)\right) - \cosh^{-2}\left(\lambda(R+R_0)\right)\right]. \tag{4.8}$$

$\hat{V}_{CAP}$ appeared in equation (4.1) has the following form [22, 25, 42]:

$$\hat{V}_{CAP} = V_0(R) + V_1(R)\frac{\partial}{\partial R} + V_2(R)\frac{\partial^2}{\partial R^2}, \tag{4.9}$$

where

$$V_1(R) = \frac{\hbar^2}{Mf^3(R)}\frac{\partial f(R)}{\partial R}. \tag{4.10}$$

$$V_2(R) = \frac{\hbar^2}{2M}(1 - f^{-2}(R)). \tag{4.11}$$

and

$$V_0(R) = \frac{\hbar^2}{4M}f^{-3}(R)\frac{\partial^2 f}{\partial R^2} - \frac{5\hbar^2}{8M}f^{-4}(R)\left(\frac{\partial f}{\partial R}\right)^2. \tag{4.12}$$

Only two electronic states i.e. the ground ($1s\sigma_g$) and the first excited repulsive ($2p\sigma_u$) states are considered [7]. The block structure of the Floquet Hamiltonian $[(\hat{H}_f)_{\alpha n,\beta m}]$ is given as [7, 73]:

$$H^F = \begin{pmatrix} \ddots & & & & & \\ & A+4\omega I & B & 0 & 0 & \\ & B^T & A+2\omega I & B & 0 & \\ & 0 & B^T & A & B & \\ & 0 & 0 & B^T & A-2\omega I & \\ & 0 & 0 & 0 & B^T & A-4\omega I \\ & & & & & \ddots \end{pmatrix}$$

where

$$A = \begin{pmatrix} T_R + U_1[F(R)] + \hat{V}_{CAP} & \frac{1}{2}\vec{\mu}_{12}[F(R)] \cdot \vec{A}_0 \\ \frac{1}{2}\vec{\mu}_{21}[F(R)] \cdot \vec{A}_0 & T_R + U_2[F(R)] + \hat{V}_{CAP} - \omega I \end{pmatrix}$$

and

$$B = \begin{pmatrix} 0 & 0 \\ \frac{1}{2}\vec{\mu}_{12}[F(R)] \cdot \vec{A}_0 & 0 \end{pmatrix}$$

Here, T_R stands for the kinetic energy operator. To put the matrices into suitable form to apply PEM, A is transformed as A=C+D. Where,

$$C = \begin{pmatrix} T_R + U_1[F(R)] + \hat{V}_{CAP} & 0 \\ 0 & T_R + U_2[F(R)] + \hat{V}_{CAP} - \omega I \end{pmatrix}$$

and

$$D = \begin{pmatrix} 0 & \frac{1}{2}\vec{\mu}_{12}[F(R)] \\ \frac{1}{2}\vec{\mu}_{21}[F(R)] & 0 \end{pmatrix}$$

Here we define a matrix H_0^F and μ_0^F as follows:

$$H_0^F = \begin{pmatrix} \ddots & & & & & \\ & C + 4\omega I & 0 & 0 & 0 & \\ & 0 & C + 2\omega I & 0 & 0 & \\ & 0 & 0 & C & 0 & \\ & 0 & 0 & 0 & C - 2\omega I & \\ & 0 & 0 & 0 & 0 & C - 4\omega I \\ & & & & & \ddots \end{pmatrix}$$

$$\mu_0^F = \begin{pmatrix} \ddots & & & & & \\ & D & B & 0 & 0 & 0 \\ & B^T & D & B & 0 & 0 \\ & 0 & B^T & D & B & 0 \\ & 0 & 0 & B^T & D & B \\ & 0 & 0 & 0 & B^T & D \\ & & & & & \ddots \end{pmatrix}$$

Now H^F can be written as

$$H^F = H_0^F + \mu_0^F \cdot \vec{A}_0$$

Diagonalization of the complex general matrix H^F will give the necessary quasienergies (ϵ) and the eigen vectors ψ_L and ψ_R at the initial field amplitude $\vec{A}_0$. H^F depends linearly on the field amplitude $\vec{A}_0$. More importantly these equations are in a suitable form to apply the parametric equations of motion (PEM) with respect to the field amplitude (A_0) as described in the next section.

4.2 Parametric equations of motion formulation

Consider an eigen value problem

$$\bar{\bar{H}}\bar{C}_i{}^R = \bar{C}_i{}^R E_i,$$

$$(\bar{C}_i{}^L)^T \bar{\bar{H}} = E_i (\bar{C}_i{}^L)^T,$$

where $\bar{\bar{H}}$ depends linearly on λ as

$$\bar{\bar{H}} = \bar{\bar{H}}_0 + \lambda \bar{\bar{V}},$$

where $\bar{\bar{H}}_0$ and $\bar{\bar{V}}$ are λ independent matrices and $\bar{C}_i^R$, $\bar{C}_i^L$ are the respective right and left eigen vectors of the complex general matrix $\bar{\bar{H}}$ having complex eigen values E_i. Superscript T stands for transpose. $\bar{C}_i^R$ and $\bar{C}_i^L$ follows the relationship

$$(\bar{C}_i^L)^T \bar{C}_i^R = 1.$$

Following the derivation of Rabitz and co-workers [38] evolution of eigen values (E) and eigen vectors (C) as a function of the linear perturbation parameter λ is given as (derivation is given in section **1.4.1**):

$$\frac{\partial E_n}{\partial \lambda} = V_{nn}, \tag{4.13}$$

$$\frac{\partial C_i^R}{\partial \lambda} = -\sum_{j \neq i} \frac{C_j^R V_{ji}}{E_j - E_i}, \tag{4.14}$$

$$\frac{\partial C_i^L}{\partial \lambda} = -\sum_{j \neq i} \frac{C_j^L V_{ij}}{E_j - E_i}, \tag{4.15}$$

$$\frac{\partial V_{nn}}{\partial \lambda} = 2\sum_{m \neq n} \frac{V_{nm} V_{mn}}{E_n - E_m}, \tag{4.16}$$

$$\frac{\partial V_{mn}}{\partial \lambda} = \sum_{l \neq m,n} V_{ml} V_{ln} \left(\frac{1}{E_n - E_l} + \frac{1}{E_m - E_l} \right) + \frac{V_{mn} V_{mm}}{E_n - E_m} + \frac{V_{mn} V_{nn}}{E_m - E_n}. \tag{4.17}$$

Equations 4.13 to 4.17 are collectively called PEM. For the application of PEM to the photodissociation of H_2^+, V_{mn} is defined as

$$V_{mn} = (C_m^L)^T(\lambda) \mu_0^F C_n^R(\lambda). \tag{4.18}$$

Equations 4.13, 4.16 and 4.17 form a close set of equations and can be integrated to get the eigen values. However, equations 4.13 to 4.17 can be integrated to obtain the eigen functions also.

4.3 Results and discussion

We have considered H_2^+ molecule as a test case for the PEM implementation. The necessary potential energy surface and dipole matrix are given by Chu et al [7]. The resulting Hamiltonian is constructed in the Fourier Grid method [37]. PEM are integrated numerically using a fifth-order Runge-Kutta integrator. Before integrating the PEM through amplitude space, it is important to determine the appropriate initial conditions [i.e., the quasienergies (ϵ), V_{ij} matrix elements, and eigen vectors (C_i^R and C_i^L)] at some chosen field amplitude (A_0). We have determined this initial condition by diagonalizing the H^F matrix at an initial field amplitude of 0.001 a.u. [22, 23] Kinetic energy operator and SES terms are calculated as shown by Karlsson [25]. The resonances are calculated by diagonalizing this Hamiltonian. A LAPACK subroutine for general complex matrix diagonalization is used. The real part (E_r) of the eigen value provides the position of the resonances and the reciprocal of its imaginary part (Γ) is proportional to the life time of the resonances. Using the SES method, we have computed the complex quasi-vibrational energies of H_2^+ for wavelength (Λ) 2660 Å at the field amplitude of 0.001 a.u. We have used 151 basis functions to achieve very high convergence for both E_r and Γ i.e., further increase in the number of basis functions will not make any perceivable difference to the plots. After the diagonalization of the SES Hamiltonian (equation 4.1) ϵ, C_i^R and C_i^L are immediately obtained at the field amplitude of 0.001 a.u. Using equation 4.18 the matrix elements are obtained. After that PEM are integrated as a function of field amplitude. Advantage of the use of PEM lies in the fact that we can trace different resonance states as a function of the laser field parameters. Otherwise in the diagonalization method , the eigen values are rearranged every time and that information is lost. In Fig. 4.1, we have compared the results obtained from diagonalizing the SES Hamiltonian and from solving the PEM at A_0=0.005 a.u. and 0.016 a.u. respectively. Fig. 4.1 (a) shows both the SES and PEM results at A_0=0.005 a.u. The PEM results and the SES results are denoted by open circles and filled squares respectively. From this plot it is clear that

Table 4.1: Resonances for the H_2^+ molecule at the amplitude 0.005 a.u. (A) Diagonalization results. (B) PEM results.

	Real part	Imaginary part
A	-0.0979 1810 6764	-0.0000 0000 0057
B	-0.0979 1810 6764	-0.0000 0000 0057
A	-0.0878 1919 7791	-0.0000 0003 0681
B	-0.0878 1919 7791	-0.0000 0003 0681
A	-0.0784 0769 2351	-0.0000 0277 5872
B	-0.0784 0769 2351	-0.0000 0277 5872
A	-0.0697 5868 9992	-0.0001 4564 2534
B	-0.0697 5868 9992	-0.0000 4564 2534
A	-0.0512 0459 4501	-0.0004 9230 0987
B	-0.0512 0459 4501	-0.0000 9230 0987
A	-0.0451 5017 9920	-0.0005 6939 2679
B	-0.0451 5017 9920	-0.0005 6939 2679
A	-0.0375 2587 0797	-0.0000 5956 5339
B	-0.0375 2587 0797	-0.0000 5956 5339

the results obtained from PEM integration are of good concordance with the direct diagonalization results. Similarly, Fig. 4.1(b) shows both the SES and PEM results at A_0=0.016 a.u. From this plot also, it is clear that the results overlap precisely for higher field amplitude also.

A better comparison of resonances obtained from the diagonalization method and the PEM at amplitudes of 0.005 and 0.016 a.u. respectively is made in tables 4.1 and 4.2 respectively. The resonances are calculated by using θ_0=0.09 in both the cases. From these tables it is clear that the results obtained from PEM integration are of good concordance with the direct diagonalization results.

In Fig. 4.2, we have compared the results obtained from different paths i.e., Moiseyev path (4.3), Taylor path (4.5) and MSES path (4.6). Results obtained from MSES and Taylor paths are symbolized by open circles and squares respectively. However, results obtained from Moiseyev path are symbolized by filled diamonds.

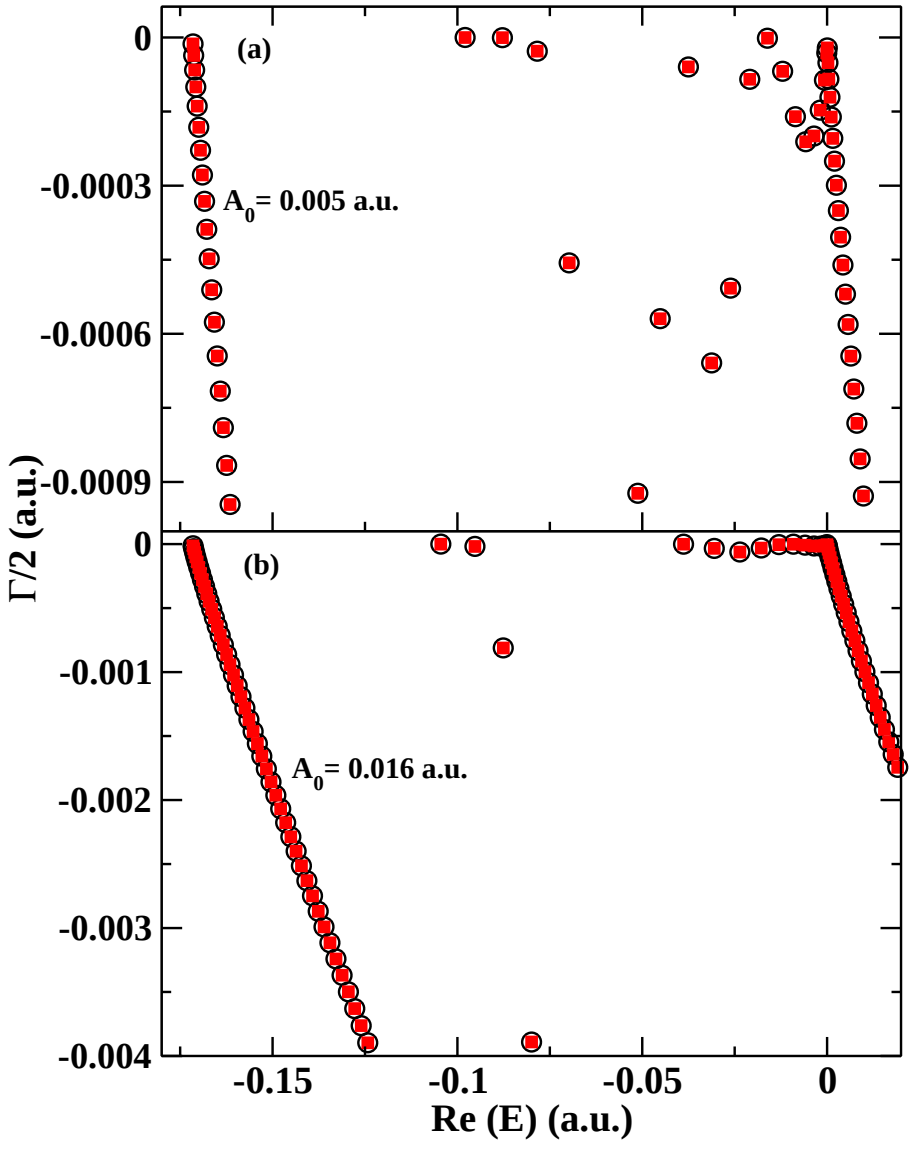

Figure 4.1: Plot of results obtained from diagonalizing the SES Hamiltonian and from solving the PEM at A_0=0.005 a.u. and 0.016 a.u.

Table 4.2: Resonances for the H_2^+ molecule at the amplitude 0.016 a.u. (A) Diagonalization results. (B) PEM results.

	Real part	Imaginary part
A	-0.1044 9914 1253	-0.0000 0000 2713
B	-0.1044 9914 1249	-0.0000 0000 2714
A	-0.0952 5837 2098	-0.0000 1795 4268
B	-0.0952 5837 2097	-0.0000 1795 4271
A	-0.0875 8958 9308	-0.0008 1134 9093
B	-0.0875 8958 9306	-0.0008 1134 9093
A	-0.0388 1717 7505	-0.0000 0056 1234
B	-0.0388 1717 7489	-0.0000 0056 1248
A	-0.0305 1884 2508	-0.0000 3339 1918
B	-0.0305 1884 2460	-0.0000 3339 1855
A	-0.0235 8824 2653	-0.0000 6191 3252
B	-0.0235 8824 2646	-0.0000 6191 3260
A	-0.0178 1029 1460	-0.0000 3061 9647
B	-0.0178 1029 1458	-0.0000 3061 9654

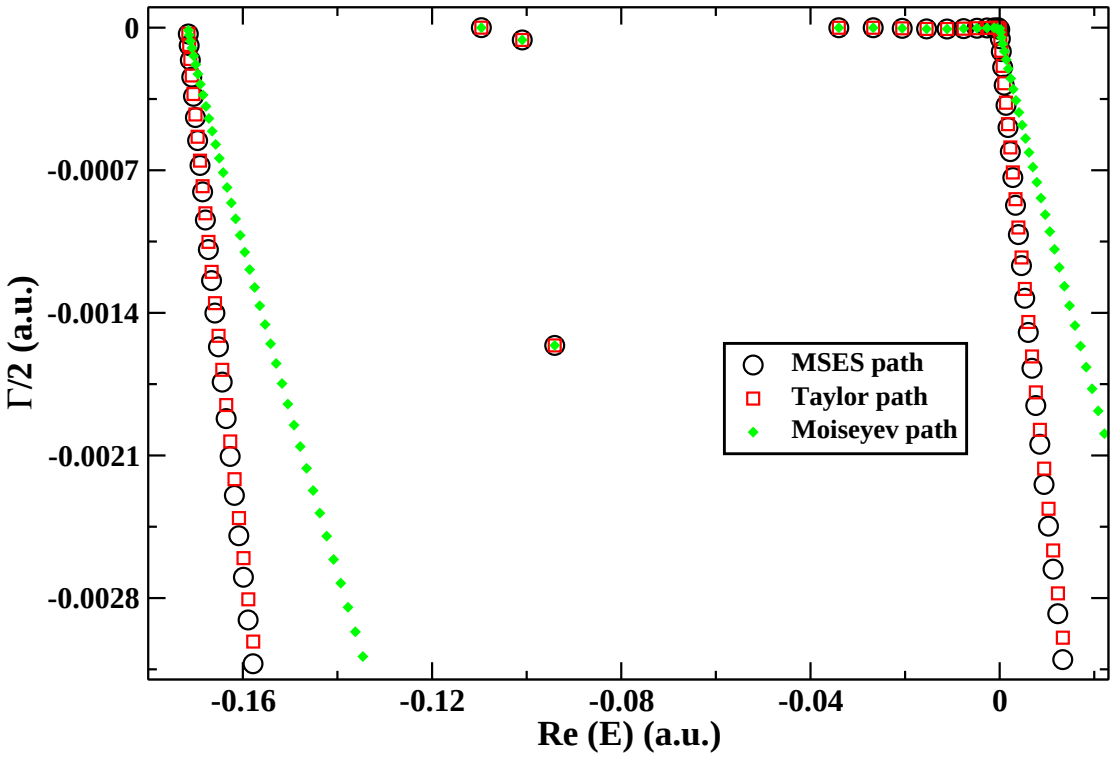

Figure 4.2: Plot of the positions of resonances [i.e., real part of the quasienergies (Re (E))] vs. width of resonances ($\Gamma/2$) for three different scaling paths.

From this plot it is clear that the results are of good concordance. The results are obtained at an amplitude of 0.02 a.u. and θ_0=0.09.

We have tested the stability of the resonances obtained from both the diagonalization and the PEM methods in Fig. 4.3. Resonances have been calculated for θ_0=0.09, 0.12 and 0.15. The PEM results are denoted by open circles (θ_0=0.09), squares (θ_0=0.12) and diamonds (θ_0=0.15) respectively. The diagonalization results are denoted by pluses (θ_0=0.09), crosses (θ_0=0.12) and stars (θ_0=0.15) respectively. From this plot it is clear that the resonances are stable enough with respect to θ_0.

In Fig. 4.4, we have plotted the positions of resonances [i.e., real part of the

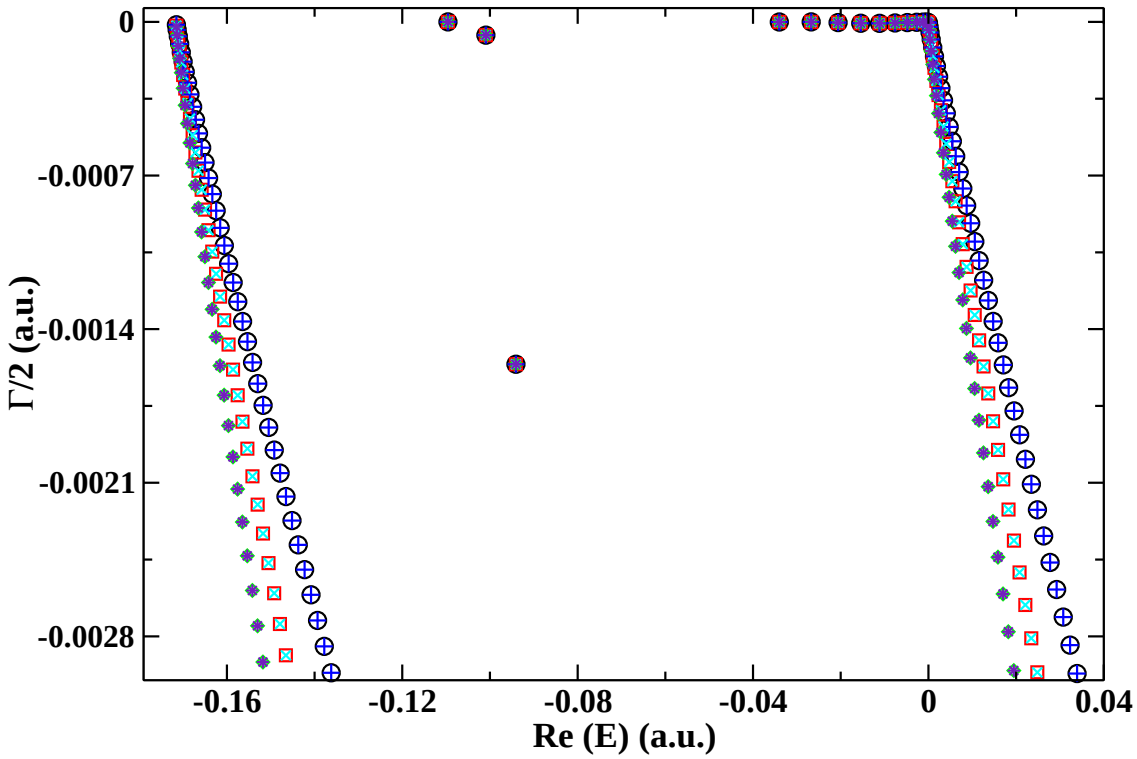

Figure 4.3: Plot of the positions of resonances [i.e., real part of the quasienergies (Re (E))] vs. width of resonances ($\Gamma/2$) for a range of θ_0 values.

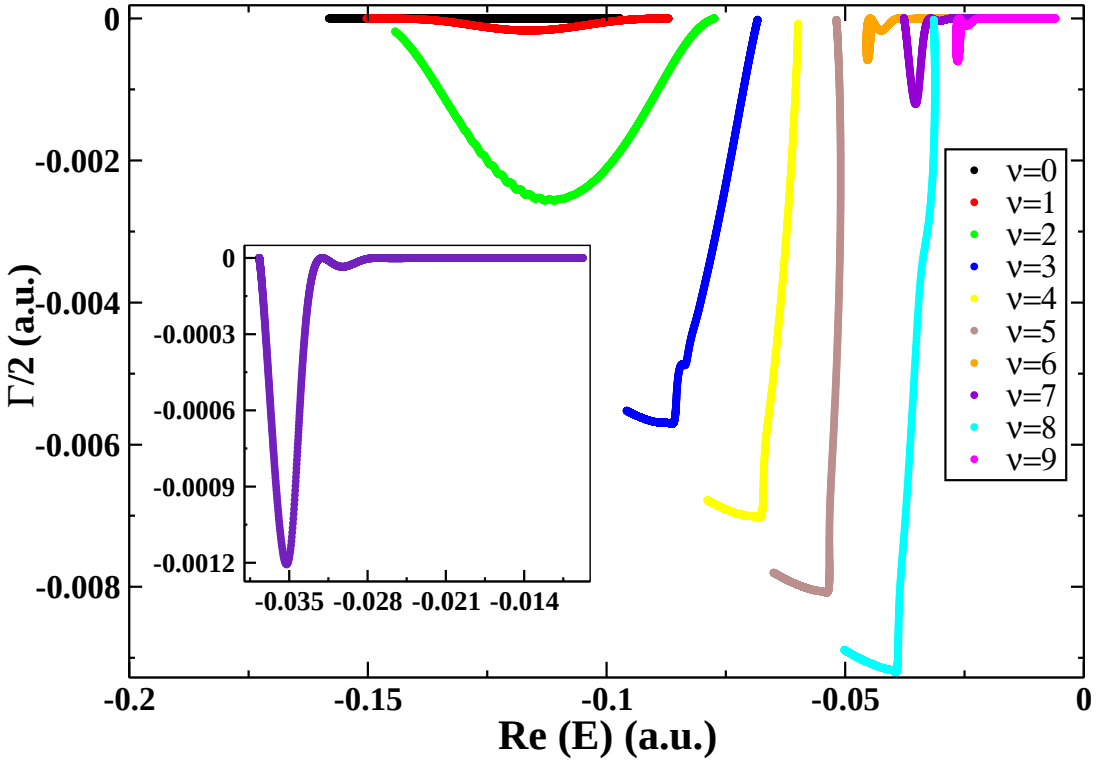

Figure 4.4: Plot of the positions of resonances [i.e., real part of the quasienergies (Re (E))] vs. width of resonances ($\Gamma/2$) for a range of A_0.

quasienergies (Re (E))] vs width of resonances ($\Gamma/2$) for a range of A_0 (i.e., A_0 goes over 0.001 a.u. to 0.5 a.u.). Here we have plotted ν=0, 1, 2 to 9^{th} vibrational states of H_2^+ as a function of A_0. From this plot one can notice that at the higher A_0 value the 6^{th}, 7^{th} and 9^{th} vibrational state becomes the bound state. It can be clearly seen in case of the 7^{th} vibrational state plotted in the inset of the Fig. 4.2. It is impossible to obtain this information from the diagonalization method (see Fig. 2.9 in **Chapter 2**) [22]. This is an example of a bound state among continuum states.

In Fig. 4.5, we have plotted the wavefunction (Ψ) of ν=7^{th} resonance state corresponding to $\mid g\rangle$, $\mid e\rangle$ Floquet channels for different A_0 values. Here solid line

represents Ψ corresponding to $\mid g\rangle$ Floquet channel whereas broken line represents Ψ corresponding to $\mid e\rangle$ Floquet channel. In Fig. 4.5 (a), Ψ of ν=7^{th} resonance state corresponding to $\mid g\rangle$, $\mid e\rangle$ Floquet channels at A_0=0.006 a.u. have been plotted. Similarly, Ψ of ν=7^{th} resonance state corresponding to $\mid g\rangle$, $\mid e\rangle$ Floquet channels at A_0=0.011, 0.016, 0.021, 0.026 and 0.031 a.u. have been plotted in Fig. 4.5 (b), 4.5 (c), 4.5 (d), 4.5 (e) and 4.5 (f) respectively. From Fig. 4.5 (a), it is clear that Ψ resembles a resonance state. As the field amplitude increases in Fig. 4.5 (c), it is clear that Ψ possesses a tail extending into continuum. However, as the field amplitude increases to 0.021 a.u. [Fig. 4.5 (f)], Ψ becomes the bound state in a continuum. This state doesn't contain any tail going into continuum. It looks like a bound state having vibrational quantum number one (i.e., ν=1) as it contains only one node. ν=6^{th} resonance state behaves like a ground vibrational state. ν=8^{th} resonance state becomes a part of the continuum at higher field amplitude and ν=9^{th} resonance state again behaves like a bound state at higher field amplitude. These states are localized on the well formed by the adiabatic potential energy curves around the one photon crossing at higher field amplitude [22]. The main advantage of the implementation of the PEM is that we can easily trace different resonance states accurately as a function of laser field amplitudes. Though computationally matrix diagonalization is 10 times faster than the PEM method, the efficiency of the PEM lies in the fact that the variation of a specific resonance state with respect to a range of field parameters (i.e., amplitude and frequency) can be easily traced which is shown in Fig. 4.4. This is because in PEM the line number of a particular resonance state remains fixed in output whereas in the matrix diagonalization it is rearranged every time. In Fig. 2.4 of **chapter 2** [22], it will be impossible to connect a resonance at two different amplitudes when lots of resonances are close to each other. It would be impossible to recognize if there was an avoided crossing or a crossing in case of diagonalization method. One reason for PEM being slow is the very high accuracy demanded during the propagation of the equations as is evident from the two tables in discussion.

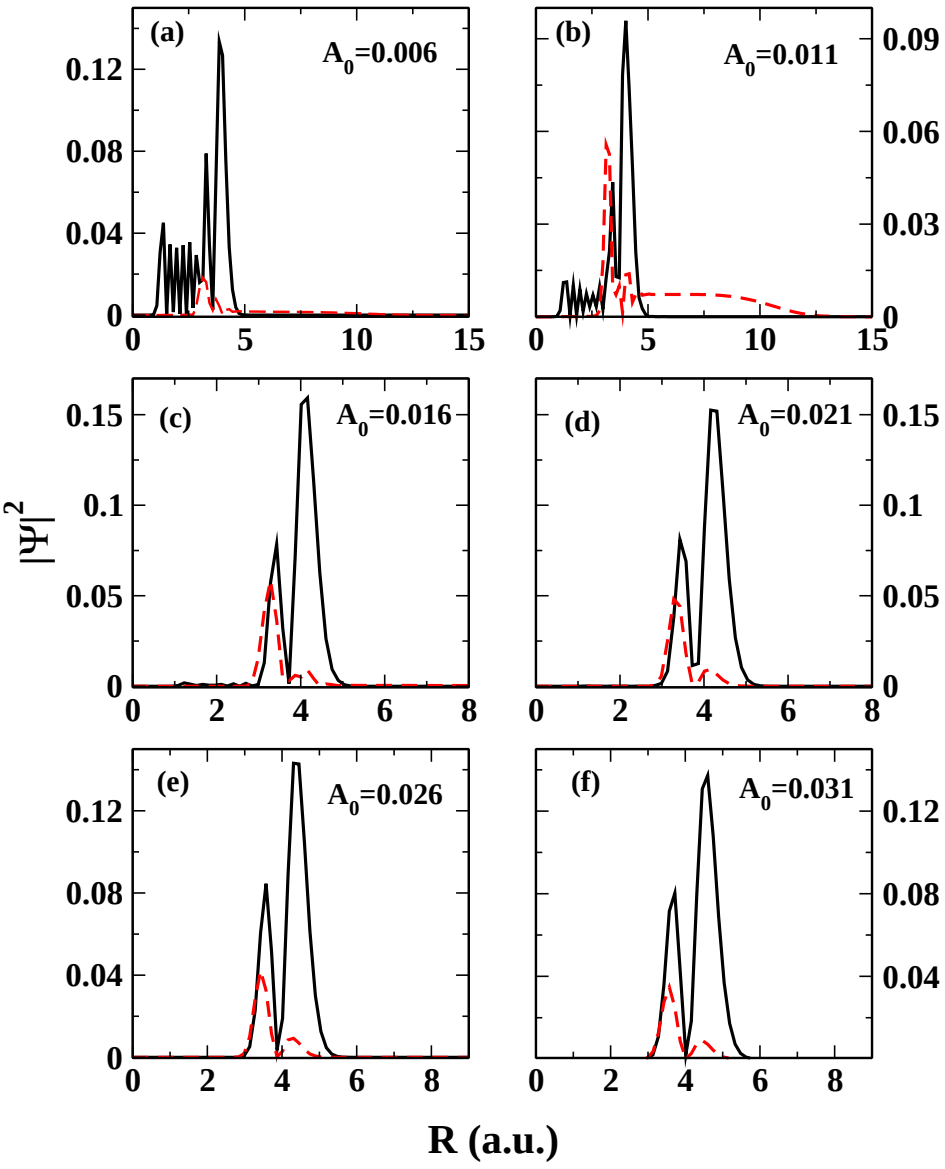

Figure 4.5: Plot of the wavefunction (Ψ) of ν=7^{th} resonance state corresponding to $|\, g\rangle$, $|\, e\rangle$ Floquet channels for different A_0 values.

4.4 Concluding remarks

We have applied parametric equations of motion (PEM) to study photodissociation dynamics of H_2^+. The resonances are extracted using smooth exterior scaling method. This is the first application of PEM to non-Hermitian Hamiltonian that includes resonances and the continuum. Here we have studied how the different resonance states behave with respect to the change in field amplitude. The advantage of this method is that one can easily trace the different states that are changing as the field parameter changes. In summary, we are able to trace different vibrational states as a function of field amplitude. We can see very clearly that some higher lying vibrational states become bound states in continuum at higher field amplitudes.

Chapter 5

APPLICATION OF PARAMETRIC EQUATIONS OF MOTION TO STUDY THE RESONANCE COALESCENCE IN H_2^+

Recently, occurrence of coalescence point was reported in H_2^+ undergoing multiphoton dissociation in strong laser field. The occurrence of coalescence of two eigenstates, or in other words, exceptional points [44], in physical system viz. H_2^+ described by non-Hermitian quantum mechanics has been an emerging topic of interest [16]. The decay rate Γ or life time $\frac{\hbar}{\Gamma}$ of H_2^+ depends on the ground vibrational state and is associated with the complex energy spectrum $(\mathrm{E} - \mathrm{i}\frac{\Gamma}{2})$ of the molecular Hamiltonian dressed by laser. Values of E and Γ depend on the laser parameters [wavelength (Λ) and field amplitude (A_0)]. At some specific laser field parameters i.e., Λ and A_0, two different resonances, which are obtained from two different field free vibrational states of H_2^+, might coalesce [32]. Coalescence of two or more states actually represents the crossing

of these states having same symmetry within the framework of the non-Hermitian formalism (which is forbidden in the standard Hermitian formalism). At the crossing point the eigenvalues are degenerate but respective eigen functions coalesce. The points (Λ, A_0) in parameter space where two mutually orthogonal resonance states coalesce into a single self-orthogonal state are usually called exceptional points (EPs) [16,27]. Suppose, we label two orthogonal eigen functions as ψ_1 and ψ_2 which coalesce when Λ=Λ_{bp} where "bp" stands for branch point. At the coalescence point,

$$\psi_1(r;\Lambda_{bp}) = \psi_2(r;\Lambda_{bp}) = \psi_{bp}(r)$$

and

$$\langle\psi_{bp}|\psi_{bp}\rangle = 0. \tag{5.1}$$

The eigen function $\psi_1(r;\Lambda_{bp})$ for which the equation 5.1 is satisfied is referred as a self-orthogonal state. Coalescence seems to be inaccessible to experiment as a branch point in the spectrum is removed by any infinitesimally small perturbation. Hence it may be considered as a mathematical object rather than a physical one. In case of complex rotated Hamiltonian of He atom, Moiseyev et al. analyzed theoretically the self-orthogonality phenomenon [45]. In the coalescence phenomenon while going around a closed path in the parameter space that includes coalescing parameters, coalescing states are exchanged with each other. In other words, coalescing state at the starting point becomes another coalescing state and vice versa after completion of the closed path (i.e., wavefunction and eigen values of the starting state acquire the wavefunction and eigen values of the other state after returning back to the same point). That is what we have studied here.

Let us briefly out line the theoretical formulation of the H_2^+ photodissociation problem. The laser field couples only with the two electronic states i.e., the ground ($1s\sigma_g$) and the first excited repulsive ($2p\sigma_u$) states [7]. The molecular Hamiltonian is

expressed with the help of a 2×2 matrix:

$$H(t) = \begin{pmatrix} T_R + U_1(R) & \mu[F(R)]A_0\cos(\omega t) \\ \mu[F(R)]A_0\cos(\omega t) & T_R + U_2(R) \end{pmatrix}$$

Here R stands for the vibrational coordinate, μ is the dipole operator, and $T_R = -\frac{\hbar^2}{2M_{H_2^+}}\frac{\partial^2}{\partial R^2}$ stands for the usual vibrational kinetic energy operator, with $M_{H_2^+}$ as the reduced mass. U_i (i=1,2) represents the potential energy surfaces of the two electronic states respectively (given in **Chapter 2**). Here $\mu[F(R)]$ is the dipole operator and A_0 and ω is the amplitude and frequency of the laser respectively. We have used the standard length gauge. The expression of dipole operator in the length gauge is given in equation 2.6 of **Chapter 2**. Since the Hamiltonian [H(t)] is time periodic having period T=$\frac{2\pi}{\omega}$, Floquet ansatz is applied. Chu and co-workers [7] had calculated the complex quasienergies by diagonalizing the complex scaled Floquet Hamiltonian whose size in the Fourier Grid basis depends upon the number of grid points (N), the number of electronic surfaces involved in photodissociation (m) and the number of photons absorbed (n). The dimension of the Hamiltonian matrix will be $(mN \times mN)$ for a single photon excitation. The form of Floquet Hamiltonian ($\hat{H}_f$) derived by Chu and co-workers [7] including the SES absorbing term [22–25] is given by,

$$\begin{aligned}(\hat{H}_f)_{\alpha n,\beta m} = &\left[\frac{\hat{P}^2}{2M} + U_{\alpha,\beta}(F(R)) + n\hbar\omega + \hat{V}_{CAP}\right]\delta_{\alpha\beta}\delta_{nm} \\ &+ \left[\frac{1}{2}\vec{\mu}_{\alpha\beta}(F(R)).\vec{A}_0\right]\delta_{(n,m=n\pm1)}\cdot(1-\delta_{\alpha\beta}),\end{aligned} \tag{5.2}$$

where α and β denote the electronic states and indices m and n go over the Fourier expansion of Floquet vector ranging from $+\infty$ to $-\infty$. Here, F(R) is the path in the complex coordinate plane defined as [63],

$$\frac{\partial F}{\partial R} = 1 + [\exp(i\theta_0) - 1]\, g(R)$$

where g(R) is varied from 0 to 1 smoothly around the point R=R_0 and θ_0 and λ are the scaling parameters. We have used modified smooth exterior scaling (MSES) path [23]. To study the coalescence phenomenon, we have applied parametric equations of motion (PEM). In this Chapter, we have tried to implement PEM jointly with modified smooth exterior scaling method (MSES) to study the coalescence of H_2^+. We have calculated the complex quasi-vibrational energies of H_2^+ for initial wavelength (Λ=Λ_{start}) at the field amplitude of 0 (A_0=0) a.u. by using the MSES method. At A_0=0, we will get only bound states and continuum by diagonalizing $(\hat{H}_f)_{\alpha n,\beta m}$ given in equation 5.2. These states become resonance states at higher A_0 value. We have assigned quantum number to these resonance states i.e., a resonance state starting from n^{th} field free state will be called n^{th} resonance state and this quantum number will remain fixed to these resonance states as integration of the PEM is performed and the resonance states change as a function of the parameters i.e., Λ and A_0. At low intensity, one can recognize the resonance states by looking at the wavefunctions and matching that with field free state. But at higher intensity, wavefunctions might look very different from field free state and as a result it will be impossible to assign them a quantum number by inspection. But PEM keeps track of these quantum numbers throughout the integration. We have carried out integration of PEM from A_0=0 to the starting point of the closed loop that encircles the EP to keep assignment of the quantum numbers to different resonance states fixed. We have followed a rectangular loop from the starting point. In this closed loop, PEM are integrated in the amplitude domain by keeping frequency fixed. Then integration of PEM is carried out in the frequency domain for a fixed amplitude. After that, PEM is again integrated in the amplitude domain (reverse direction) for a fixed frequency. Finally in order to complete the closed loop and to come back to the starting point, integration of PEM is carried out in the frequency domain (reverse direction) by keeping amplitude fixed. This whole process encircles the EPs. In case of coalescence, if two states having quantum number 'i' and 'j', coalesce then i^{th} and j^{th} state will exchange their

properties after completion of the closed loop in parameter space. Formulation of PEM in the amplitude domain as well as the necessary theoretical formulation of the H_2^+ photodissociation problem is extensively discussed in **Chapter 3**. Formulation of PEM in the frequency domain are outlined here. The block structure of the Floquet Hamiltonian $[(\hat{H}_f)_{\alpha n,\beta m}]$ (given in equation 5.2) is given as [7]:

$$H^F = \begin{pmatrix} \ddots & & & & & \\ & A+4\omega I & B & 0 & 0 & 0 \\ & B^T & A+2\omega I & B & 0 & 0 \\ & 0 & B^T & A & B & 0 \\ & 0 & 0 & B^T & A-2\omega I & B \\ & 0 & 0 & 0 & B^T & A-4\omega I \\ & & & & & \ddots \end{pmatrix}$$

where

$$A = \begin{pmatrix} T_R + U_1[F(R)] + \hat{V}_{CAP} & \frac{1}{2}\vec{\mu}_{12}[F(R)] \cdot \vec{A}_0 \\ \frac{1}{2}\vec{\mu}_{21}[F(R)] \cdot \vec{A}_0 & T_R + U_2[F(R)] + \hat{V}_{CAP} - \omega I \end{pmatrix}$$

and

$$B = \begin{pmatrix} 0 & 0 \\ \frac{1}{2}\vec{\mu}_{12}[F(R)] \cdot \vec{A}_0 & 0 \end{pmatrix}$$

Here T_R stands for the kinetic energy operator. To put the matrices into suitable form in order to apply PEM, A is transformed as A=C+D·ω. Where,

$$C = \begin{pmatrix} T_R + U_1[F(R)] + \hat{V}_{CAP} & \vec{\mu}_{12}[F(R)] \cdot \vec{A}_0 \\ \vec{\mu}_{21}[F(R)] \cdot \vec{A}_0 & T_R + U_2[F(R)] + \hat{V}_{CAP} \end{pmatrix}$$

and

$$D = \begin{pmatrix} 0 & 0 \\ 0 & -I \end{pmatrix}$$

Here we define a matrix H_0^F and P as follows:

$$H_0^F = \begin{pmatrix} \ddots & & & & & \\ & C & B & 0 & 0 & 0 \\ & B^T & C & B & 0 & 0 \\ & 0 & B^T & C & B & 0 \\ & 0 & 0 & B^T & C & B \\ & 0 & 0 & 0 & B^T & C \\ & & & & & \ddots \end{pmatrix}$$

$$P = \begin{pmatrix} \ddots & & & & & \\ & 4I + D & B & 0 & 0 & 0 \\ & B^T & 2I + D & B & 0 & 0 \\ & 0 & B^T & D & B & 0 \\ & 0 & 0 & B^T & -2I + D & B \\ & 0 & 0 & 0 & B^T & -4I + D \\ & & & & & \ddots \end{pmatrix}$$

Now H^F can be written as

$$H^F = H_0^F + P \cdot \omega$$

Diagonalization of the complex general matrix H^F will give the necessary quasienergies (ϵ) and the left and right eigen vectors c_L and c_R respectively at the initial laser

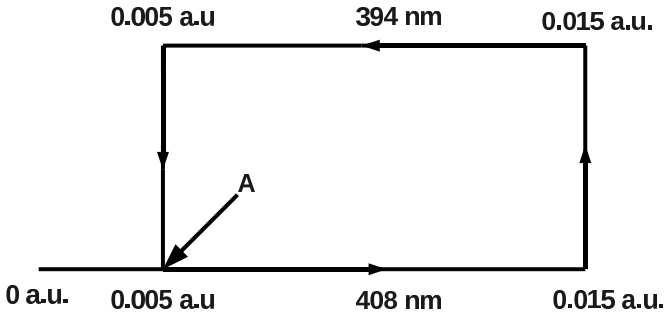

Figure 5.1: Encircling of EP occuring around wavelength (Λ) 401 nm and amplitude (A_0) $\sim$ 0.0121 a.u. Here A denotes the starting point of the closed loop.

field wavelength (Λ_{start}). H^F depends linearly on ω.

5.1 Results and discussion

The necessary potential energy surface and transition dipole moment are given by Bunkin et al. [4] and are given in the previous Chapters. The resulting Hamiltonian is constructed in the Fourier Grid method [37]. Diagonalization procedure and the integration of the PEM are exactly same as those given in **Chapter 4**. Here, we have varied the Hamiltonian parameters (i.e., Λ and A_0) along a closed path which encircles the EPs at 401 nm and amplitude 0.0121 a.u. and 442 nm and amplitude 0.0106 a.u. respectively as reported by Lefebvre et al [32]. We have computed the complex quasi-vibrational energies of H_2^+ by using the MSES method. We have included three channels in the calculation i.e., the value of n in equation 5.2 goes from -3 to +2. We have shown in **Chapter 2** that n=3 is sufficient enough to get convergent results [22]. We have used 151 basis functions to achieve very high convergence for both E_r and Γ i.e., further increase in the number of basis functions will not make any perceivable difference to the plots. After the diagonalization of the SES Hamiltonian $(\hat{H}_f)_{\alpha n,\beta m}$, ϵ, C_i^R and C_i^L are immediately obtained. The encircling path of the EP is shown in Fig. 5.1 and Fig. 5.2.

In figure 5.1, we have shown the closed path to encircle the EP occuring between

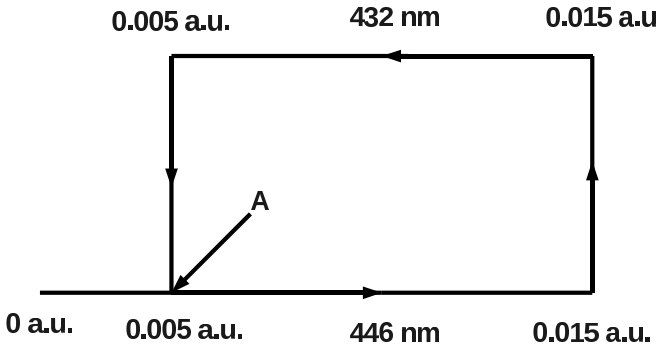

Figure 5.2: Encircling of EP occuring around wavelength (Λ) 442 nm and amplitude (A_0) $\sim$ 0.0106 a.u. Here A denotes the starting point of the closed loop.

9^{th} and 10^{th} resonance state around wavelength (Λ) 401 nm and at an amplitude (A_0) $\sim$ 0.0121 a.u. as reported by Lefebvre and co-workers [32]. We have used initial and final amplitudes as 0.005 a.u. and 0.015 a.u. respectively and initial wavelength (Λ_{start}) and final wavelength (Λ_{end}) as 408 and 394 nm to encircle the EP around Λ=401 nm and A_0=0.0121 a.u. From this encircling we have found that 9^{th} (ν=8) resonance state coalesces with a continuum state and 10^{th} (ν=9) resonance state coalesces with another continuum state. This fact is supported by Fig. 5.3 where change in positions of resonances [i.e., real part of the quasienergies (Re (E))] vs. widths of resonances ($\Gamma/2$) as A_0 changes from 0 a.u. to 0.015 a.u. are plotted. Broken lines represent continuum and solid lines represent bound states. Each curve corresponds to a particular Λ. From this figure it is evident that the continuum state is bending toward the left and the 9^{th} resonance state is bending toward the right with the increase in amplitude in the wavelength range 394 to 404 nm. But after wavelength 406 nm, both the states have changed their direction as if they have exchanged their characteristics and this is the point where coalescence occurs. We can say that coalescence occurs in the range of 404 to 406 nm.

Similarly, in Fig. 5.4, we have shown the occurrence of coalescence between 10^{th} (ν=9) resonance state and the continuum state that coalesces with ν=9. In the range of Λ=396 to 398 nm, 10^{th} resonance state and the continuum state exchange their

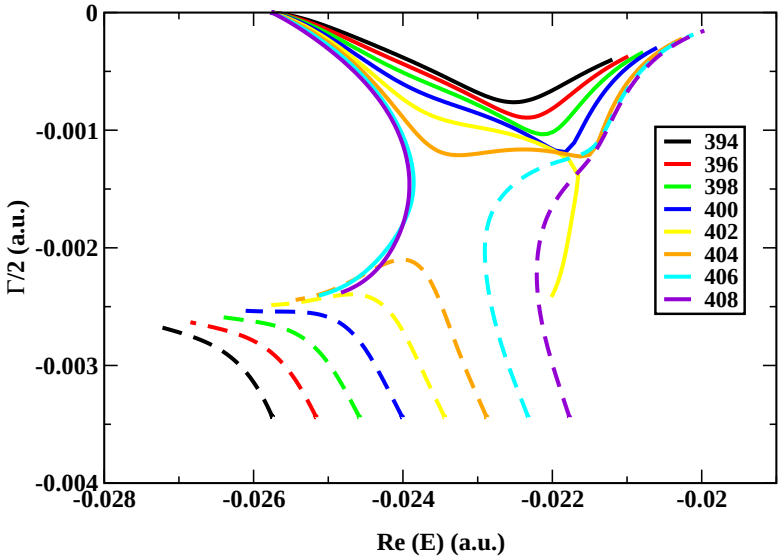

Figure 5.3: Plot of 9^{th} resonance state (solid line) and the continuum state that coalesces with 9^{th} resonance state (broken line) corresponding to different wavelength as depicted in the legend box. On each curve $\Gamma/2$ and Re(E) change as amplitude changes from 0.0 a.u. to 0.015 a.u.

behaviour. In Fig. 5.5, Re(E) and $\Gamma/2$ of ν=9^{th} resonance state and the continuum state coalescing with ν=9^{th} state are plotted for Λ=396 nm and Λ=398 nm. The coalescence will occur in between these two Λ. For Λ=396 nm and lower value (not shown), the two coalescing states cross each other. On the other hand, for Λ=398 nm, the two coalescence states undergo avoided crossing and it will increase as Λ takes higher and higher value (not shown). As one goes closer to the coalescence point, this avoided crossing between the coalescing states become narrower and narrower. Fig. 5.5 is an illustration of how two coalescing states exchange their behaviour at the EP.

In a similar manner, Fig. 5.2 shows the encircling of the EP occuring around Λ=442 nm and at A_0 ~0.0106 a.u. between 8^{th} and 9^{th} resonance states as calculated by Lefebvre et al [32]. From this encircling we have found that 8^{th} (ν=7) resonance state coalesces with a continuum state and 9^{th} (ν=8) resonance coalesces with another continuum state. This fact is supported by Fig. 5.6 where change in positions of

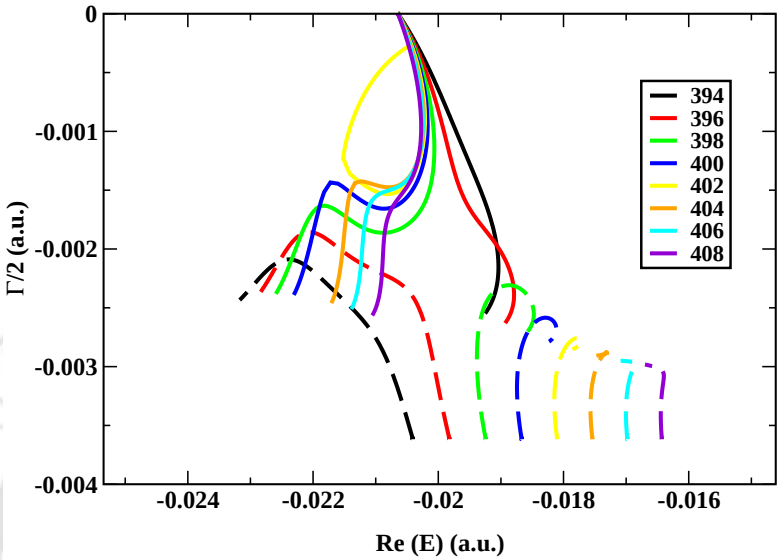

Figure 5.4: Plot of 10^{th} resonance state (solid line) and the continuum state that coalesces with 10^{th} resonance state (broken line) corresponding to different wavelength as depicted in the legend box. On each curve $\Gamma/2$ and Re (E) change as amplitude changes from 0.0 a.u. to 0.015 a.u.

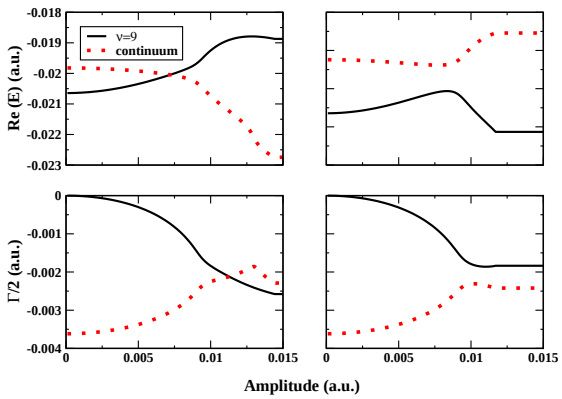

Figure 5.5: Re (E) (top panel) and $\Gamma/2$ (bottom panel) of 10^{th} resonance state (dotted line) and the continuum state that coalesces with 10^{th} resonance state (solid line) is plotted as a function of amplitude at Λ=396 nm (left plot) and 398 nm (right plot). Note that coalescence will occur in between these two Λ.

resonances [i.e., real part of the quasienergies (Re (E))] vs. widths of resonances ($\Gamma/2$) as A_0 changes from 0 a.u. to 0.015 a.u. are plotted. In the range of Λ=442 to 444 nm, 8^{th} resonance state and the continuum state exchange their behaviour. Similarly, in Fig. 5.7, we have shown the occurrence of coalescence between 9^{th} (ν=8) resonance state and the continuum state that coalesces with ν=8 in the range of Λ=434 to 436 nm. In Fig. 5.8, Re(E) and $\Gamma/2$ of $\nu=8^{th}$ resonance state and the continuum state coalescing with $\nu=8^{th}$ state are plotted for Λ=434 nm and Λ=436 nm. The coalescence will occur in between these two Λ. The two coalescing states cross each other for Λ=434 nm or lower value (not shown). On the other hand, for Λ=436 nm, the two coalescence states undergo avoided crossing and it will increase as Λ takes higher and higher value (not shown). However, in the vicinity of the coalescence point, this avoided crossing between the coalescing states become narrower and narrower. Like Fig. 5.5, Fig. 5.8 also illustrates how two coalescing states exchange their behaviour at the coalescence point.

Further, as we decrease the number of grid points from 151 to 121, a different coalescence picture appears. When we have carried out the encircling of the EP (which is supposed to occur at $\Lambda \sim 401$ nm and A_0=0.0121 a.u.) for Λ ranging from 394 to 408 nm, we have found that 9^{th} resonance state (ν=8) coalesces with 10^{th} resonance state (ν=9) around Λ=400 nm. Similarly, encircling of the EP (which is supposed to occur $\sim$ 442 nm and A_0=0.0106 a.u.) for Λ ranging from 432 nm to 446 nm has shown an occurrence of coalescence between 8^{th} (ν=7) resonance state and 9^{th} (ν=8) resonance state around Λ=440 nm. We will like to point out that Lefebvre et al. [32] has reported the same results what we have got when 121 grid points instead of 151 grid points are used. To test the convergence of our results, we have increased the number of grid points from 151 to 171. This increase in number of grid points does not make any noticeable difference to the results.

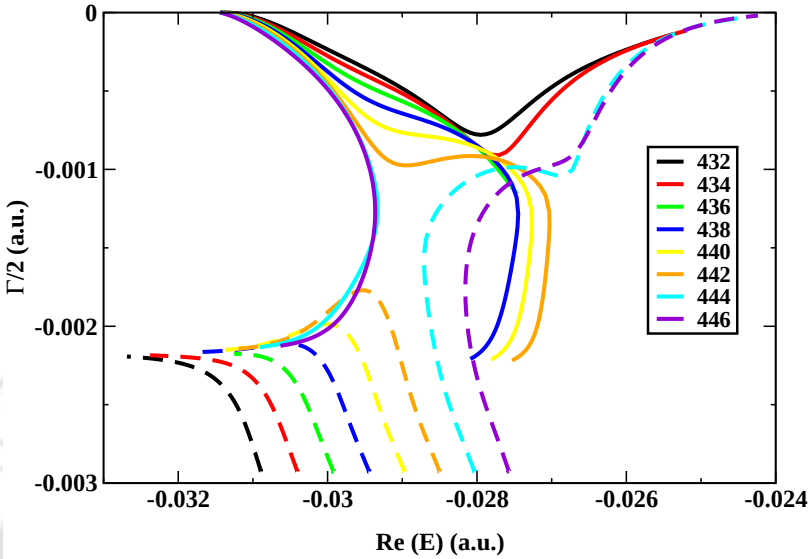

Figure 5.6: Plot of 8^{th} resonance state (solid line) and the continuum state that coalesces with 8^{th} resonance state (broken line) corresponding to different wavelength as depicted in the legend box. On each curve $\Gamma/2$ and Re (E) change as amplitude changes from 0.0 a.u. to 0.015 a.u.

5.2 Concluding remarks

In summary, we have applied parametric equations of motion (PEM) and smooth exterior scaling method to study the coalescence phenomenon of H_2^+. The advantage of PEM is that one can easily trace different resonance states that are changing as the field parameter changes. We have carried out the encircling of the exceptional points in parameter space, where Λ and A_0 are chosen as parameters. From encircling, we have found that coalescence occurs between one bound and one continuum state when the number of grid points used are 151. The same results are obtained when the number of grid points are increased to 171. However, as we decrease the number of grid points from 151 to 121, we have found the occurrence of coalescence between two bound states.

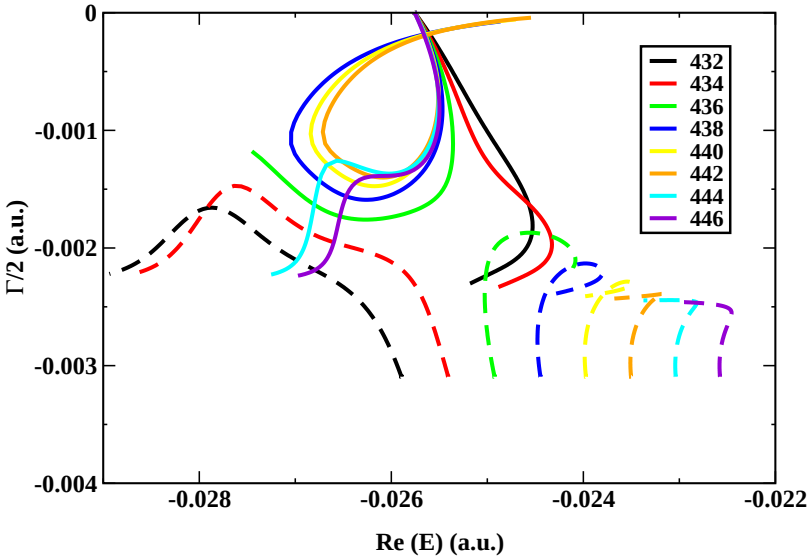

Figure 5.7: Plot of 9^{th} resonance state (solid line) and the continuum state that coalesces with 9^{th} resonance state (broken line) corresponding to different wavelength as depicted in the legend box. On each curve $\Gamma/2$ and Re (E) change as amplitude changes from 0.0 a.u. to 0.015 a.u.

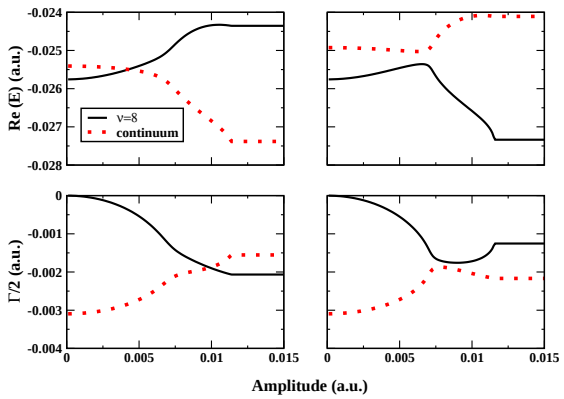

Figure 5.8: Re (E) (top panel) and $\Gamma/2$ (bottom panel) of 9^{th} resonance state (dotted line) and the continuum state that coalesces with 9^{th} resonance state (solid line) is plotted as a function of amplitude at Λ=434 nm (left plot) and 436 nm (right plot). Note that coalescence will occur in between these two Λ.

Chapter 6

CONCLUSIONS

The hydrogen molecular ion H_2^+ being the simplest molecule, is of fundamental importance in molecular physics. The interaction of H_2^+ with intense ultrafast laser light has revealed novel phenomena viz. bond softening and bond hardening in light induced molecular potentials [56]. Implementation of the non-Hermitian quantum mechanics is most useful in exploration of the resonance phenomena, where particles are temporarily trapped by the potential. Owing to the exponential divergence of the asymptotes of the resonance states, it is essential to carry out complex scaling transformations of the Hamiltonian. After this transformation resonance states become square integrable as bound states in the standard formalism. Through out this thesis, we have applied smooth exterior scaling (SES) transformations to calculate accurately different resonance states of H_2^+ molecular ion. We have applied Floquet ansatz. We have found that the rate of dissociation of resonance states increases as we employ more than one Floquet block. We have reported that even at low intensity (10^{11} W/cm^2), multiphoton transitions play a dominant role in the photodissociation process. We have also found "vibrationally trapped" states for higher laser field amplitude.

With the help of SES, it is possible to generate reflection free complex absorbing potential (RFCAP). However, it is always necessary to improve the quality of these

RFCAPs. We have modified the existing conventional SES (CSES) method to get a better absorption of the artificial reflections occuring at the grid boundary during propagation of the wavepacket. This new modified SES method is much more efficient in absorbing the wavepacket near the grid boundary compared with the CSES method. We have shown that with this modified SES (MSES) method also, it is possible to calculate accurately different resonance states of H_2^+. We have reported that the MSES method gives more accurate results than the CSES method. Moreover, the MSES method requires much lesser grid points for scaling to get accurate results.

In this thesis, we have reported the importance of parametric equations of motion (PEM) in photodissociation dynamics of H_2^+ molecular ion. In case of PEM, Schrödinger equation was solved explicitly only once and the solutions at other parameter values were obtained by integrating a set of ordinary differential equations through the parameter space of the Hamiltonian. The efficiency of the PEM lies in the fact that the variation of a specific resonance state with respect to a range of field parameters (i.e., amplitude and frequency) can be easily traced. The behaviour of different resonance states with respect to the change in field amplitude has been reported.

The resonances of H_2^+ are calculated accurately by applying PEM along with the SES method. Resonance coalescence in H_2^+ has also been studied with the help of PEM. We have explained the coalescence with the help of the encircling of the exceptional point in parameter space where wavelength (Λ) and amplitude (A_0) are treated as parameter. We have reported the occurrence of coalescence between field free vibronic state and continuum state for higher number of grid points. However, for lower number of grid points, it has been found that coalescence occurs between field free vibronic states.

Bibliography

[1] P. Agostini, F. Fabre, G. Mainfray, G. Petite, and N. K. Rahman. *Phys. Rev. Lett.*, 42:1127, 1979.

[2] E. Balslev and J. M. Combes. *Commun. Math. Phys.*, 22:280, 1971.

[3] P. H. Bucksbaum, A. Zavriyev, H. G. Muller, and D. W. Schumacher. *Phys. Rev. Lett.*, 64:1883, 1990.

[4] F. V. Bunkin and I. I. Tugov. *Phys. Rev. A*, 8:601, 1973.

[5] S. I. Chu. *Chem. Phys. Lett.*, 64:178, 1979.

[6] S. I. Chu and W. P. Reinhardt. *Phys. Rev. Lett.*, 39:1195, 1977.

[7] Shih-I Chu. *J. Chem. Phys.*, 94:7901, 1991.

[8] D. T. Colbert and W. H. Miller. *J. Chem. Phys.*, 96:1982, 1992.

[9] N. Elander and E. Yarevsky. *Phys. Rev. A*, 57:3119, 1998.

[10] S. Feuerbacher, T. Sommerfeld, R. Santra, and L. S. Cederbaum. *J. Chem. Phys.*, 118:6188, 2003.

[11] J. Y. Ge and J. Z. H. Zhang. *J. Chem. Phys.*, 108:1429, 1998.

[12] A. Giusti-Suzor, X. He, O. Atabek, and F. H. Mies. *Phys. Rev. Lett.*, 64:515, 1990.

[13] A. Giusti-Suzor and F. H. Mies. *Phys. Rev. Lett.*, 68:3869, 1992.

[14] Peter Gross, Ashish Gupta, Deepa B. Bairagi, and Manoj K. Mishra. *Chem. Phys. Lett.*, 236:8, 1995.

[15] Ashish K. Gupta, Peter Gross, Deepa B. Bairagi, and Manoj K. Mishra. *Chem. Phys. Lett.*, 257:658, 1996.

[16] W. D. Heiss. *Phys. Rev. E*, 61:929, 2000.

[17] S. Hofferberth, B. Fischer, T. Schumm, J. Schmiedmayer, and I. Lesanovsky. *Phys. Rev. A*, 76:013401, 2007.

[18] J. D. Morgan III and B. Simon. *J. Phys. B*, 14:L167, 1981.

[19] E. K. Irish. *Phys. Rev. Lett.*, 99:173601, 2007.

[20] G. Jolicard and E. J. Austin. *Chem. Phys. Lett.*, 121:106, 1985.

[21] G. Jolicard and G. Billing. *J. Chem. Phys.*, 97:997, 1992.

[22] Dhruba Jyoti Kalita and Ashish K. Gupta. *J. Chem. Phys.*, 133:1343031, 2010.

[23] Dhruba Jyoti Kalita and Ashish K. Gupta. *J. Chem. Phys.*, 134:094301, 2011.

[24] Dhruba Jyoti Kalita and Ashish K. Gupta. *J. Chem. Phys.*, 134:224309, 2011.

[25] H. O. Karlsson. *J. Chem. Phys.*, 109:9366, 1998.

[26] H. O. Karlsson. *J. Chem. Phys.*, 108:3849, 1998.

[27] T. Kato. *Perturbation theory for linear operators*. Springer, New York, 1966.

[28] R. Kosloff and D. Kosloff. *J. Comput. Phys.*, 63:363, 1986.

[29] P. Kruit, J. Kimman, H. G. Muller, and M. J. van der Wiel. *Phys. Rev. A*, 28:248, 1983.

[30] C. Leasure, K. F. Milfeld, and R. E. Wyatt. *J. Chem. Phys.*, 74:6197, 1981.

[31] C. Leasure and R. E. Wyatt. *J. Chem. Phys.*, 73:4439, 1980.

[32] R. Lefebvre, O. Atabek, M. Sindelka, and N. Moiseyev. *Phys. Rev. Lett.*, 103:123003, 2009.

[33] N. Lipkin, N. Moiseyev, and E. Brandas. *Phys. Rev. A*, 40:549, 1989.

[34] P O Lowdin. *Adv. Quantum. Chem.*, 19:87, 1988.

[35] T. S. Luk and C. K. Rhodes. *Phys. Rev. A*, 38:6180, 1988.

[36] U. Manthe, T. Seideman, and W. H. Miller. *J. Chem. Phys.*, 99:10078, 1993.

[37] C. C. Marston and Gabriel G. Balint-Kurti. *J. Chem. Physics*, 91:3571, 1989.

[38] David A. Mazziotti, Manoj K. Mishra, and Herschel A. Rabitz. *J. Phys. Chem.*, 99:112, 1995.

[39] C. W. McCurdy and T. N. Rescigno. *Phys. Rev. Lett.*, 41:1364, 1978.

[40] J. Miller, L. Li, W. A. Chupka, and S. D. Colson. *J. Chem. Phys.*, 88:2975, 1988.

[41] N. Moiseyev. *Phys. Rev. A*, 20:814, 1979.

[42] N. Moiseyev. *Phys. Rep.*, 302:211, 1998.

[43] N. Moiseyev. *J. Phys. B: At. Mol. Opt. Phys.*, 31:1431, 1998.

[44] N. Moiseyev. *Non-Hermitian Quantum Mechanics*. Cambridge University Press, New York, 2011.

[45] N. Moiseyev and S. Friedland. *Phys. Rev. A*, 22:618, 1980.

[46] N. Moiseyev and J. O. Hirschfelder. *J. Chem. Phys.*, 88:1063, 1988.

[47] J. G. Muga, J. P. Palao, B. Navarro, and I. L. Egusquiza. *Phys. Rep.*, 395:357, 2004.

[48] D. Neuhauser. *J. Chem. Phys.*, 100:9272, 1994.

[49] D. Neuhauser and M. Baer. *J. Chem. Phys.*, 90:4351, 1989.

[50] D. Neuhauser and M. Baer. *J. Chem. Phys.*, 91:4651, 1989.

[51] Cleanthes A. Nicolaides and Donald R. Beck. *Phys. Lett.*, 65A:11, 1978.

[52] Anna Nissen, H. O. Karlsson, and Gunilla Kreiss. *J. Chem. Phys.*, 133:054306, 2010.

[53] D. Normand and J. Morellec. *J. Phys. B*, 21:L625, 1988.

[54] P. Pechukas. *Phys. Rev. Lett.*, 51:943, 1983.

[55] J. Perie, G. Jolicard, and J. P. Killingbeck. *J. Chem. Phys.*, 98:6344, 1993.

[56] J. H. Posthumus. *Rep. progress. Phys.*, 67:623, 2004.

[57] W. P. Reinhardt. *Annu. ReV. Phys. Chem.*, 33:223, 1982.

[58] T. N. Rescigno, M. Baertschy, D. Byrum, and C. W. McCurdy. *Phys. Rev. A*, 55:4253, 1997.

[59] U. V. Riss and H-D. Meyer. *J. Phys.B: At. Mol. Opt. Phys.*, 26:4503, 1993.

[60] U. V. Riss and H. D. Meyer. *J. Phys. B*, 26:4503, 1993.

[61] U. V. Riss and H. D. Meyer. *J. Phys. B*, 28:1465, 1995.

[62] U. V. Riss and H. D. Meyer. *J. Phys. B*, 31:2279, 1998.

[63] N. Rom, E. Engdahl, and N. Moiseyev. *J. Chem. Phys.*, 93:3413, 1990.

[64] Naomi Rom, Nurit Lipkin, and Nimrod Moiseyev. *Chem. Phys.*, 151:199, 1991.

[65] Y. Sajeev, R. Santra, and S. Pal. *J. Chem. Phys.*, 123:204110, 2005.

[66] W. R. Salzman. *Phys. Rev. A*, 10:461, 1974.

[67] K. Sandig, H. Figger, and T. W. Hansch. *Phys. Rev. Lett.*, 85:4876, 2000.

[68] R. Santra and L. S. Cederbaum. *Phys. Rep.*, 368:1, 2002.

[69] T. Seideman and W. H. Miller. *J. Chem. Phys.*, 96:4412, 1992.

[70] O. Shemer, D. Brisker, and N. Moiseyev. *Phys. Rev. A*, 71:032716, 2005.

[71] B. Simon. *Phys. Lett. A*, 36:23, 1971.

[72] B. Simon. *Phys. Lett.*, 71A:211, 1979.

[73] D. J. Tannor. *Introduction To Quantum Mechanics: A Time-Dependent Perspective*. University Science Books, Sausalito, California, 2007.

[74] J. R. Taylor. *Scattering Theory: The Quantum Theory of NonrelatiVistic Collisions*. Wiley and Sons, New York, 1972.

[75] D. A. Telnov and S. I. Chu. *Phys. Rev. A*, 59:2864, 1999.

[76] X. Yang and J. Burgdorfer. *Phys. Rev A*, 48:83, 1993.

[77] T. Yukawa. *Phys. Lett.*, A116:227, 1986.

[78] Raya Zavin, Ilya Vorobeichik, and Nimrod Moiseyev. *Chem. Phys. Lett.*, 288:413, 1998.

[79] D. H. Zhang and J. Z. H. Zhang. *J. Chem. Phys.*, 101:1146, 1994.

Publications

1. Dhruba Jyoti Kalita and Ashish K. Gupta, Application of smooth exterior scaling method to study the time dependent dynamics of H_2^+ in intense laser field, *J. Chem. Phys.* (2010), **133**, 134303.

2. Dhruba Jyoti Kalita and Ashish K. Gupta, Use of modified smooth exterior scaling method as an absorbing potential and its application, *J. Chem. Phys.* (2011), **134**, 094301.

3. Dhruba Jyoti Kalita, Akshay Rao, Ishir Rajvanshi, and Ashish K. Gupta, Application of parametric equations of motion to study the laser induced multiphoton dissociation of H_2^+ in intense laser field, *J. Chem. Phys.* (2011), **134**, 224309.

4. Dhruba Jyoti Kalita and Ashish K. Gupta, Laser-induced multiphoton dissociation of H2+ as a function of the field frequency using parametric equations of motion, *Phys. Rev. A* (2012), **85**, 033413.

5. Dhruba Jyoti Kalita and Ashish K. Gupta, Application of parametric equations of motion to study the resonance coalescence in H_2^+, **To be submitted**.

Vitae

Dhruba Jyoti Kalita was born in Pacharia, India. He obtained his Bachelors in Chemistry from B. Borooah College, Guwahati and completed Masters in Chemistry from Gauhati University. Under the supervision of Dr. Ashish Kumar Gupta, he started his research career at the Department of Chemistry, IITG - with the application of non-Hermitian quantum mechanics to smaller systems viz. H_2^+. His current research interests include study of resonance states of H_2^+ molecule by application of smooth exterior scaling technique and parametric equations of motion.